Title: Brawn before bite in endemic Asian mammals after the end-Cretaceous extinction

Authors:

Z. Jack Tseng[1,2,5]*, Qian Li[3]**, Suyin Ting[2,4]

Affiliations:

[1]Department of Integrative Biology and Museum of Paleontology, University of California, Berkeley; California 94720, U.S.A.

[2]Department of Vertebrate Paleontology, Natural History Museum of Los Angeles County; California 90007, U.S.A.

[3]Institute of Vertebrate Paleontology and Paleoanthropology, Chinese Academy of Sciences; Beijing 100044, China

[4]Museum of Natural Science, Louisiana State University; Baton Rouge, Louisiana 70803, U.S.A.

[5]Lead Contact

*Correspondence: zjt@berkeley.edu

**Correspondence: liqian@ivpp.ac.cn

Summary: The first 10 million years (Myr) following the Cretaceous-Paleogene (K-Pg) mass extinction marked a period of global greenhouse conditions and dramatic rise of placental mammals. Because ~80% of known terrestrial sections capturing post-K-Pg mammal recovery come from North America, a substantial knowledge gap exists in the tempo and mode of recovery in Asia, where only 3% of global sites are located and most contain species found nowhere else. We show that isolated Paleocene placental assemblages from China (1) exhibited high mean tooth size and disparity early in the Paleocene, (2) shifted in their dental shape in parallel with regional and global environmental changes later in the Paleocene, and (3) achieved maximum dental shape-performance covariation near the end of the first 10 Myr post-K-Pg. This ‘brawn before

bite' transformation, coupled with prolonged dental shape versus performance variability, favors a scenario whereby many living orders of placental mammals were borne out of phenotypically and functionally plastic ancestral assemblages, including those in tropical south China, during the Paleocene.

Main Text:

The Cretaceous-Paleogene (K-Pg) mass extinctions accelerated the formation of modern-day global biota. In particular, the more than 6,000 species of living placental mammals trace their origins to the diversification of major orders around or after the K-Pg boundary [1–3]. Different hypotheses (for example: early rise, suppression, and late rise) about the timing of their adaptive radiation have been proposed [1,4,5]. Regardless of the diversification scenarios favored by the competing explanations, the Paleocene epoch (66-56 Myr ago) has been highlighted as among the most critical time interval for establishing the macroevolutionary parameters of the placental adaptive radiation [6,7] (but see [5]). However, substantial asymmetry exists in the quantity and quality of terrestrial fossil records that document the first 10 Myr of the 'Age of Mammals', with ~80% of known terrestrial K-Pg boundary sections worldwide occurring in North America [8]. Earliest Paleocene mammals are not known from Europe [9,10], rendering detailed reconstructions of post-K-Pg recovery in that continent difficult. The post-K-Pg fossil assemblages from Asia have hitherto not been considered in analyses of post-K-Pg recovery dynamics [11].

The North American fossil record suggests that post-K-Pg mammal taxonomic diversity recovery was relatively rapid; most occurred within the first ~0.3 to 1 Myr of the Paleocene epoch [12–17]. This initial placental mammal diversification was driven by archaic groups (i.e., stem placental/eutherian lineages and extinct placental subgroups), followed by the first appearance of many modern orders during two peak hyperthermal events in the past 66 Myr, at the end-Paleocene and early Eocene climatic maxima, respectively [18,19].

Distinct from these taxonomic recovery patterns, high selectivity of mammalian ecomorphological extinction across the K-Pg boundary indicates a primary productivity filter at the start of the Cenozoic Era (66 Myr ago to the present) [20]. Additionally, the first 10 Myr of mammalian brain evolution after the K-Pg was marked by niche partitioning along a size gradient; endocranial traits reflecting more complex sensory processing did not appear until the Eocene (56 Myr ago). This phenomenon has been termed the 'brawn before brains' hypothesis [21]. A similar pattern in initial size-driven diversification followed by expansion of ecomorphological disparity is also observed in mammal jaws, indicating

a general dynamic across phenotypic systems [22]. Whether this mode of evolution, whereby size disparity increase precedes other ecomorphological traits, should be understood as a global phenomenon during the post-K-Pg placental radiation remains untested, in large part because no such analyses have centered on non-North American continental fossil mammal records.

A major challenge with expanding analyses of post K-Pg recovery to Paleocene mammal assemblages elsewhere in the world is the stratigraphically limited nature of early Cenozoic sequences that produce fossil mammals. In Asia, Paleocene localities in China represent the best studied to date [11]. From the earliest Paleocene, highly regional and endemic faunas are known from a handful of sedimentary basins (Fig. S1A). Among the recorded faunal elements, only the archaic placental clades Anagalida and Pantodonta are consistently sampled across the major subdivisions of the Paleocene [11]. An additional complication with ecomorphological analysis of these early mammals is the uncertainty in their dietary ecology, as they are beyond the reach of conventional phylogenetic bracketing approaches to dietary reconstruction. Phenomic analysis of the placental radiation supports insectivory as the ancestral diet of the hypothetical placental ancestor, but uncertainty in the post K-Pg availability of insects and plants in some regions leave some doubt as to the accuracy and scope of this ancestral state reconstruction [1]. Herein we treat the archaic Paleocene taxa in our analyses as having uncharacterized diets rather than categorizing them as insectivores, herbivores, or carnivores.

We investigated dental topography-performance shifts and timing of ecomorphological diversification by developing and leveraging the largest dataset to date of Paleocene Asian mammal assemblages. Our analyses focused on placental mammals from three of the most fossiliferous and biogeographically isolated Paleocene sedimentary sequences in paleotropical Asia: The Nanxiong, Qianshan, and Chijiang Basins in present-day south China [23–27] (Fig. S1). We generated a new phenotypic dataset of 200 Asian Paleocene mammal teeth using high-resolution microcomputed tomography and laser scanning, capturing 37 species endemic to low-latitude east Asia and which are brought to bear on K-Pg recovery dynamics for the first time (Data S1-S2). Teeth are among the most well-preserved parts of fossil mammals, and the fact that they

interface directly with the environment through mastication makes them suitable elements for studying potential ecology-morphology linkages. We used dental topographical traits ~~dentitions~~ as ~~ecological~~ indicators of ecomorphological diversity [28] and examined temporal shifts in tooth crown complexity, curvature, and height. We additionally assessed the association of topographical traits with tooth crown mechanical performance in terms of deformation resistance using topographic and simulation analyses. Our dataset spans the Paleocene, the first 10 Myr of the Cenozoic, enabling us to test the hypothesis that dental topography and tooth puncturing and shearing performance linkages showed delayed niche expansion relative to mean body size and size disparity during this initial period of post-K-Pg mammal recovery in Asia.

Dental traits paralleled Paleocene global and regional environmental conditions

We found that dental topographic trait variability in Paleocene mammals in south China tracked global and regional climatic changes despite stasis in high-level taxonomic composition over the course of the first 10 Myr after the K-Pg transition (Fig. 1). Dental height and sharpness variability were low in the beginning and end of the time interval, with a peak in the middle Paleocene. This pattern is observed both when dentitions are considered as pooled samples through time, and particularly driven by the lower dentition (Fig. S5; note that upper teeth display the opposite pattern). In contrast, elevated low-level taxonomic turnover of genera and species within the Paleocene indicates cladogenetic shifts, rather than anagenetic adaptation, underpin this dental topographic evolution (Data S1)[11]. These findings suggest that in addition to its impact on crown group mammals, the K-Pg extinctions and subsequent climatic fluctuations played a role in filtering out archaic placental mammals with lower speciation rates in favor of rapidly speciating taxa [29].

By contrast, there is no support for significant shifts in dental topographic trait mean values from the early to the middle Paleocene for the majority of analytical iterations of clade and dental data partitions (Figs 1A, S4; Table 1; Data S7). However, in most analyses we observed a significant shift in at least one dental topographic metric from the middle to the late Paleocene (Table 1; Data S7). The larger-bodied Chinese endemic pantodont (an ungulate-like archaic placental group; “CEP”) mammals tend to increase

dental complexity (OPCR, orientation patch count rotated) and curvature (DNE, Dirichlet normal energy) whereas smaller, non-pantodonts (Chinese arctostylopids and anagalids; rodent-like archaic placental groups) in the dataset exhibited no significant dental trait~~s~~ shifts from the middle to late Paleocene (Fig. S4; Data S7). The transformation by CEPs in complexity and curvature indices relates to the capacity of teeth to resist wear and coincides with temperature and aridity increase towards the end-Paleocene thermal maximum event (Figs. 1-2). Multiple geological and geochemical proxies suggest that paleoclimate in and around the Nanxiong Basin K-Pg section in south China reflects a latitudinally much broader global tropical zone during the Paleocene [30] relative to present-day Earth, as well as rapid shifts between more versus less humid intervals during the first 10 Myr of the Cenozoic [31]. Results from feldspar-quartz (F:Q) ratios, clay mineral composition analysis, diffuse reflectance spectroscopy (DRS), stable carbon isotope analysis, and total organic carbon (TOC) analysis all support this regional paleoclimate profile [31,32]. Local climate reconstructions for the latest Cretaceous indicate relatively warm and dry intervals, followed by warm and humid climates during the earlier Paleocene, then a return to less humid but still warm conditions in the later Paleocene [32]. Chinese endemic pantodont dentitions tracked shifts in this paleoenvironmental progression.

The overall increase in dental complexity and curvature also coincided with an increase in drought-tolerant flora in south China (Fig. 2) and specifically with paleoenvironmental reconstructions in the Nanxiong Basin [33]. Palynological evidence suggests that in addition to a predominance of broad-leaved, deciduous plants mixed with a smaller percentage of conifers than in fossil localities further north [34], south China also recorded drought resistant taxa such as the maidenhair fern *Pterisisporites* in the early Paleocene Shanghu formation [35] and again in late Paleocene samples [36]. Expanded comparisons across time and space suggest fossil pollen taxa that are indicators of seasonal aridity increased from 20.3% of late Paleocene pollen samples to 34.3% of early Eocene pollen samples [36]. These shifts appeared to have stabilized by the end of the Eocene, when taxonomically modern floras became established in Asia [37]. In addition to tracking Paleocene temperature trends (Fig. 1), Asian mammal dental topography (OPCR and DNE in particular) also mimicked trends in the marine realm, where global planktonic

foraminifera records demonstrate a similar pattern in species richness curve, as well as with global $\delta^{13}C$ [38,39] and south Pacific CO_2 levels [40]. These broader associations underscore the inference that endemic Paleocene mammals in south China ~~composed~~ comprised a dynamic assemblage shifting their dental morphology in step with regional and global environmental changes during the first 10 Myr after the K-Pg mass extinctions.

We detected a shift and expansion of mammal dental morphospace in the late Paleocene (Fig. 2). An overall shift towards increased dental topographic trait magnitudes in late Paleocene samples is driven mainly by CEPs (Table 1), despite the fact that they constitute a minority of the overall data (41% of teeth) as well as late Paleocene partition (21% of teeth). Additionally, dental metric disparity is significantly higher in the late Paleocene partition than in the two preceding time bins (Table 1). This pattern is driven both by increased dental curvature and complexity (DNE & OPCR; 78-100% support in per-tooth analyses, Fig. S5) in larger-bodied CEPs and crown height (RFI) in smaller-bodied non-pantodonts, in addition to differences in disparity among the clades (Data S7, Fig. S5; bootstrapped variance for DNE, OPCR, and RFI are at least twice as large in non-pantodonts compared to CEPs, and bootstrapped range lengths returned similar patterns). This suggests that an expansion of dental disparity in the late Paleocene occurred across the size spectrum of endemic Asian mammals. Over the same time interval examined, body (tooth) size disparity and mean were higher in the early Paleocene than in subsequent time intervals (Fig. S8, Table S3; also supported by premolar 4 and upper molar partition analyses), indicating that substantial increases in the disparity of dental complexity, curvature, and height lagged behind tooth size during the Paleocene. Dog-sized CEPs such as *Bemalambda* reached sizes not seen in late Cretaceous mammals from China such as *Zhangolestes* and *Kryptobaatar*, which are shrew- to gopher-sized [41]. This suggests a ‘brawn before bite’ pattern in endemic Asian mammals, partially mirroring the endocranial and jaw functional morphology patterns identified in their North American and European counterparts [21,22]. These findings raise the possibility that an initial size-driven post-K-Pg recovery followed by ecomorphological radiation was a global phenomenon, even as regional tectonic events such as the initial collision of the Indian subcontinent with Asia and Deccan Traps volcanism influenced local mammal evolution [42,43].

184 **Topography-performance covariation underlies mammal dental shifts**

185 Within an overall pattern of increasing covariation between dental topographic
186 traits and bite performance traits across the Paleocene time intervals (Fig. 3; Table S1),
187 topographic versus performance trait variability shifted both from early to middle and from
188 middle to late Paleocene time bins (Figs S3-S4). Early Paleocene to middle Paleocene
189 DTA-FEA intra- and inter-correlations remained stable (Fig. 3B), but DTA-FEA inter-
190 correlations strengthened while intra-DTA correlations weakened in the Middle to Late
191 Paleocene transition (Fig. 3C). This transition pattern is in part due to the divergence of
192 shape-performance linkages in CEP versus non-pantodont mammals, and is particularly
193 driven by the upper and lower first molars (Figs. S9-S11). Dental topography variability
194 tracked bite performance variability in non-pantodonts through time, peaking in the middle
195 Paleocene (Fig S4D). By contrast, both intra- and inter-partition comparisons of
196 topography and performance trends in CEPs showed low correlations through time (Fig.
197 S4G). The coexistence of distinct topography-performance relationships in each time and
198 taxon partition while overall covariation between the two trait groups increases between
199 time bins is consistent with form-function decoupling [44]. Complex form-function linkages
200 generally promote evolutionary redundancy and can enhance optimization of phenotypic
201 traits when selective trade-offs are present [44–46]. The presence of functional redundancies
202 underlies the high levels of dental topographic variability in Asian Paleocene mammals.
203 Alternatively, varying degrees of independence between the two performance traits and
204 dental topographic traits analyzed could allow the two aspects of the dentition to evolve
205 in a decoupled manner (Fig. 3).

206 **South Asia as a Paleogene 'Garden of Eden' for placental mammals?**

207 Among the most consequential implications of accurately interpreting post-K-Pg
208 mammalian recovery dynamics in Asia is the ability to reconstruct the evolutionary
209 conditions during the biogeographic origination of modern placental orders. Current
210 knowledge and an overwhelming majority of data about the first post-dinosaur mammal
211 ecological communities center on North American localities [12,47], and secondarily from
212 European records [48]. Yet, the fossil records of those continents pinpoint a high turnover
213 of mammal faunas at the Paleocene-Eocene boundary, driven by the

Cretaceous/Paleocene origination of major modern mammal clades elsewhere and subsequent dispersal of those lineages to the European and North American continents, respectively. At least five living orders (Primates, Rodentia, Lagomorpha, Perissodactyla, Eulipotyphla), representing over half of mammalian species richness today, trace their evolutionary origins to Asia [18,49–51]. There is also mounting evidence that other organisms, including fish and plant lineages, followed a similar biogeographic pattern [52].

The abrupt appearance of early representatives of modern mammal lineages in North America has been formally operationalized by the 'East of Eden' model, wherein Asia is the 'Garden of Eden' and a biodiversity pump of living orders of placental mammals [53] and other organisms. Biogeographic modeling analysis of modern mammalian diversity also strongly identifies tropical south Asia, including the geographic regions occupied today by southern China, India, and southeast Asian countries, as the cradle of mammalian diversification since the Paleocene [54]. As geographically proximate faunal assemblages to the epicenter of the 'Garden of Eden' hypothesis, the endemic Paleocene mammals of the Asian paleotropics analyzed in this study exhibited a high degree of dental topographic variability while strengthening topography-performance covariation during a period of biogeographic isolation and regional and global climate changes. Such flexibility in dental form-function linkage permits 'mix and match' trait combinations rather than evolutionary transformation as a single unit, potentially enhancing the evolvability of feeding ecological traits as new environmental conditions arose [56]. This finding favors the scenario whereby many living orders of placental mammals were borne out of phenotypically and functionally plastic ancestral assemblages, including those that lived in south China, during the Paleocene [55].

We further infer from these findings that episodes of fluctuating global warming during the first 10 Myr of the Cenozoic promoted the evolution of 'all-purpose' mammalian dentitions rather than those with specialized functions (Fig. 3). This prolonged dental topographic variability tracks extended post-K-Pg floral recovery times [36,57], and suggests a 'brawn before brains' mode of placental mammal evolution may in part represent a series of correlated evolutionary shifts in sync with the steadily increasing complexity of Paleocene primary producers [20,37]. That a global signal would be detected in the

splendidly isolated south Asian Paleocene assemblage is notable, and indicates that effects of climate forcing on post-K-Pg mammal recovery may be ubiquitous, as has been predicted for Earth's ongoing rapid environmental shifts [58]. In response, Paleocene mammal clades in south China were relatively larger early on and increased covariation between dental topography and bite performance later, all the while maintaining high levels of variability in dental complexity and convexity (Fig. 1). These preconditions set the stage for the subsequent taxonomic turnover between archaic and crown lineages during the Paleogene to Neogene modernization of mammal communities [19,26]. As a primary interface against shifting food resources and the environment, the placental dentition was poised to play an outsized role in the explosive diversification following the K-Pg extinctions, with the masticatory complex having already completed the macroevolutionary transition to a mechanically stiff but phenotypically flexible jaw during the Mesozoic Era [59,60]. The end-Cretaceous extinctions and the climatic volatility that followed then set in motion the ecological release that enabled mammals to explore dental form-function to a far fuller extent in 66 Myr of the Cenozoic Era than during the preceding 150 Myr under the reign of dinosaurs. This sequence of 'brawn before bite' in tooth size, topographic, and performance evolution further refines the placental success story.

262 **References**

263 1. O'Leary, M.A., Bloch, J.I., Flynn, J.J., Gaudin, T.J., Giallombardo, A., Giannini,
264 N.P., Goldberg, S.L., Kraatz, B.P., Luo, Z.-X., and Meng, J. (2013). The placental
265 mammal ancestor and the post–K-Pg radiation of placentals. Science . *339*, 662–
266 667.

267 2. Liu, L., Zhang, J., Rheindt, F.E., Lei, F., Qu, Y., Wang, Y., Zhang, Y., Sullivan, C.,
268 Nie, W., Wang, J., et al. (2017). Genomic evidence reveals a radiation of
269 placental mammals uninterrupted by the KPg boundary. Proc. Natl. Acad. Sci.
270 *114*, E7282–E7290. 10.1073/pnas.1616744114.

271 3. Foley, N.M., Mason, V.C., Harris, A.J., Bredemeyer, K.R., Damas, J., Lewin, H.A.,
272 Eizirik, E., Gatesy, J., Karlsson, E.K., Lindblad-Toh, K., et al. (2025). A genomic
273 timescale for placental mammal evolution. Science . *380*, eabl8189.
274 10.1126/science.abl8189.

275 4. Benevento, G.L., Benson, R.B.J., Close, R.A., and Butler, R.J. (2023). Early
276 Cenozoic increases in mammal diversity cannot be explained solely by expansion
277 into larger body sizes. Palaeontology *66*, e12653.
278 https://doi.org/10.1111/pala.12653.

279 5. Grossnickle, D.M., Smith, S.M., and Wilson, G.P. (2019). Untangling the Multiple
280 Ecological Radiations of Early Mammals. Trends Ecol. Evol. *34*, 936–949.
281 https://doi.org/10.1016/j.tree.2019.05.008.

282 6. Upham, N.S., Esselstyn, J.A., and Jetz, W. (2021). Molecules and fossils tell
283 distinct yet complementary stories of mammal diversification. Curr. Biol. *31*,
284 4195–4206.

285 7. Halliday, T.J.D., Upchurch, P., and Goswami, A. (2017). Resolving the
286 relationships of Paleocene placental mammals. Biol. Rev. *92*, 521–550.
287 https://doi.org/10.1111/brv.12242.

288 8. Vajda, V., and Bercovici, A. (2014). The global vegetation pattern across the
289 Cretaceous–Paleogene mass extinction interval: a template for other extinction

events. Glob. Planet. Change *122*, 29–49.

9. Csiki-Sava, Z., Buffetaut, E., Ősi, A., Pereda-Suberbiola, X., and Brusatte, S.L. (2015). Island life in the Cretaceous-faunal composition, biogeography, evolution, and extinction of land-living vertebrates on the Late Cretaceous European archipelago. Zookeys, 1–161.

10. De Bast, E., and Smith, T. (2017). The oldest Cenozoic mammal fauna of Europe: implication of the Hainin reference fauna for mammalian evolution and dispersals during the Paleocene. J. Syst. Palaeontol. *15*, 741–785.

11. Wang, Y., Meng, J., Ni, X., and Li, C. (2007). Major events of Paleogene mammal radiation in China. Geol. J. *42*, 415–430.

12. Wing, S.L., Alroy, J., and Hickey, L.J. (1995). Plant and mammal diversity in the Paleocene to early Eocene of the Bighorn Basin. Palaeogeogr. Palaeoclimatol. Palaeoecol. *115*, 117–155.

13. Alroy, J. (1999). The fossil record of North American mammals: evidence for a Paleocene evolutionary radiation. Syst. Biol. *48*, 107–118.

14. Longrich, N.R., Scriberas, J., and Wills, M.A. (2016). Severe extinction and rapid recovery of mammals across the Cretaceous–Palaeogene boundary, and the effects of rarity on patterns of extinction and recovery. J. Evol. Biol. *29*, 1495–1512.

15. Lyson, T.R., Miller, I.M., Bercovici, A.D., Weissenburger, K., Fuentes, A.J., Clyde, W.C., Hagadorn, J.W., Butrim, M.J., Johnson, K.R., Fleming, R.F., et al. (2019). Exceptional continental record of biotic recovery after the Cretaceous–Paleogene mass extinction. Science . *366*, 977–983. 10.1126/science.aay2268.

16. Wilson, G.P. (2014). Mammalian extinction, survival, and recovery dynamics across the Cretaceous-Paleogene boundary in northeastern Montana, USA. In Through the End of the Cretaceous in the Type Locality of the Hell Creek Formation in Montana and Adjacent Areas, G. P. Wilson, W. A. Clemens, J. R. Horner, and J. H. Hartman, eds. (Geological Society of America).

17. Grossnickle, D.M., and Newham, E. (2016). Therian mammals experience an ecomorphological radiation during the Late Cretaceous and selective extinction at the K–Pg boundary. Proc. R. Soc. B Biol. Sci. *283*, 20160256. 10.1098/rspb.2016.0256.

18. Gingerich, P.D. (2010). Mammalian faunal succession through the Paleocene-Eocene Thermal MAximum (PETM) in western North America. Vertebr. Palasiat. *48*, 308–327.

19. Bowen, G.J., Clyde, W.C., Koch, P.L., Ting, S., Alroy, J., Tsubamoto, T., Wang, Y., and Wang, Y. (2002). Mammalian dispersal at the Paleocene/Eocene boundary. Science . *295*, 2062–2065.

20. Wilson, G.P. (2013). Mammals across the K/Pg boundary in northeastern Montana, U.S.A.: dental morphology and body-size patterns reveal extinction selectivity and immigrant-fueled ecospace filling. Paleobiology *39*, 429–469. DOI: 10.1666/12041.

21. Bertrand, O., Shelley, S., Williamson, T., Wible, J., Chester, S., Flynn, J., Holbrook, L., Lyson, T., Meng, J., Miller, I., et al. (2022). Brawn before brains in placental mammals after the end-Cretaceous extinction. Science . *376*, 80–85. 10.1126/science.abl5584.

22. Benevento, G.L., Benson, R.B.J., and Friedman, M. (2019). Patterns of mammalian jaw ecomorphological disparity during the Mesozoic/Cenozoic transition. Proc. R. Soc. B Biol. Sci. *286*, 20190347. 10.1098/rspb.2019.0347.

23. Chow, M., Zhang, Y., Wang, B., and Ding, S. (1977). Paleocene mammalian fauna from the Nanxiong Basin, Guangdong Province. Paleontol. Sin. New Ser. C *20*, 1–100.

24. Clyde, W.C., Tong, Y., Snell, K.E., Bowen, G.J., Ting, S., Koch, P.L., Li, Q., Wang, Y., and Meng, J. (2008). An integrated stratigraphic record from the Paleocene of the Chijiang Basin, Jiangxi Province (China): Implications for mammalian turnover and Asian block rotations. Earth Planet. Sci. Lett. *269*, 554–

564.

25. Clyde, W.C., Ting, S., Snell, K.E., Bowen, G.J., Tong, Y., Koch, P.L., Li, Q., and Wang, Y. (2010). New paleomagnetic and stable-isotope results from the Nanxiong Basin, China: implications for the K/T boundary and the timing of Paleocene mammalian turnover. J. Geol. *118*, 131–143.

26. Ting, S.-Y., Tong, Y.-S., Clyde, W.C., and Koch, P.L. (2011). Asian early Paleogene chronology and mammalian faunal turnover events. Vertebr. Palasiat. *49*, 1–28.

27. Wang, Y.-Q., Li, C.-K., Li, Q., and Li, D.-S. (2016). A synopsis of Paleocene stratigraphy and vertebrate paleontology in the Qianshan Basin, Anhui, China. Vertebr. Palasiat. *54*, 89–120.

28. Lucas, P., Constantino, P., Wood, B., and Lawn, B. (2008). Dental enamel as a dietary indicator in mammals. BioEssays *30*, 374–385. https://doi.org/10.1002/bies.20729.

29. Quintero, I., Lartillot, N., and Morlon, H. (2024). Imbalanced speciation pulses sustain the radiation of mammals. Science . *384*, 1007–1012.

30. Yin, Y., Zhang, L., Gu, X., Yin, R., Wen, Y., Jin, T., and Wang, C. (2023). High terrestrial temperature in the low-latitude Nanxiong Basin during the Cretaceous-Paleogene boundary interval. Palaeogeogr. Palaeoclimatol. Palaeoecol. *617*, 111489. https://doi.org/10.1016/j.palaeo.2023.111489.

31. Huang, H., Ma, M., Wang, M., and Liu, X. (2024). The paleoclimatic significance indicated by the Early Paleogene gray-black mudstone layers lies in Nanxiong Basin. Quat. Sci. *44*, 1250–1261.

32. Wang, Y., Li, X., Zhou, Y., and Liu, L. (2015). Paleoclimate indication of terrigenous clastic rock's component during the Late Cretaceous–Early Paleocene in the Nanxiong Basin. Acta Sedimentol. Sin. *33*, 116–123.

33. Ma, M., Liu, X., and Wang, W. (2018). Palaeoclimate evolution across the Cretaceous–Palaeogene boundary in the Nanxiong Basin (SE China) recorded by

red strata and its correlation with marine records. Clim. Past *14*, 287–302. 10.5194/cp-14-287-2018.

34. Hao, H., Ferguson, D.K., Feng, G.-P., Ablaev, A., Wang, Y.-F., and Li, C.-S. (2010). Early Paleocene vegetation and climate in Jiayin, NE China. Clim. Change *99*, 547–566.

35. Xie, Y., Wu, F., and Fang, X. (2020). A major environmental shift by the middle Eocene in southern China: Evidence from palynological records. Rev. Palaeobot. Palynol. *278*, 104226.

36. Ma, X., Jiang, H., Cheng, J., and Xu, H. (2012). Spatiotemporal evolution of Paleogene palynoflora in China and its implication for development of the extensional basins in East China. Rev. Palaeobot. Palynol. *184*, 24–35.

37. Su, T., Spicer, R.A., Li, S.-H., Xu, H., Huang, J., Sherlock, S., Huang, Y.-J., Li, S.-F., Wang, L., and Jia, L.-B. (2019). Uplift, climate and biotic changes at the Eocene–Oligocene transition in south-eastern Tibet. Natl. Sci. Rev. *6*, 495–504.

38. MacLeod, N., Ortiz, N., Fefferman, N., Clyde, W., Schulter, C., MacLean, J., Culver, S.J., and Rawson, P.F. (2000). Phenotypic response of foraminifera to episodes of global environmental change. Biot. response to Glob. Environ. Chang. last *145*, 51–78.

39. Keller, G., Mateo, P., Punekar, J., Khozyem, H., Gertsch, B., Spangenberg, J., Bitchong, A.M., and Adatte, T. (2018). Environmental changes during the Cretaceous-Paleogene mass extinction and Paleocene-Eocene thermal maximum: implications for the Anthropocene. Gondwana Res. *56*, 69–89.

40. Hollis, C.J., Naeher, S., Clowes, C.D., Naafs, B.D.A., Pancost, R.D., Taylor, K.W.R., Dahl, J., Li, X., Ventura, G.T., and Sykes, R. (2022). Late Paleocene CO2 drawdown, climatic cooling and terrestrial denudation in the southwest Pacific. Clim. Past *18*, 1295–1320. 10.5194/cp-18-1295-2022.

41. Meng, J. (2014). Mesozoic mammals of China: implications for phylogeny and early evolution of mammals. Natl. Sci. Rev. *1*, 521–542. 10.1093/nsr/nwu070.

402 42. Hu, X., Garzanti, E., Moore, T., and Raffi, I. (2015). Direct stratigraphic dating of
403 India-Asia collision onset at the Selandian (middle Paleocene, 59±1 Ma). Geology
404 *43*, 859–862.

405 43. Ma, M., Wang, M., Huang, H., and Liu, X. (2024). Terrestrial records of two
406 hyperthermal events in the Cretaceous-Paleogene boundary suggest different
407 control mechanisms. Commun. Earth Environ. *5*, 1–7.

408 44. Wainwright, P.C., Alfaro, M.E., Bolnick, D.I., and Hulsey, C.D. (2005). Many-to-
409 One Mapping of Form to Function: A General Principle in Organismal Design?
410 Integr. Comp. Biol. *45*, 256–262. 10.1093/icb/45.2.256.

411 45. Polly, P.D., Stayton, C.T., Dumont, E.R., Pierce, S.E., Rayfield, E.J., and
412 Angielczyk, K.D. (2016). Combining geometric morphometrics and finite element
413 analysis with evolutionary modeling: towards a synthesis. J. Vertebr. Paleontol.
414 *36*, e1111225.

415 46. Pollock, T.I., Deakin, W.J., Chatar, N., Milla Carmona, P.S., Rovinsky, D.S.,
416 Panagiotopoulou, O., Parker, W.M.G., Adams, J.W., Hocking, D.P., Donoghue,
417 P.C.J., et al. (2025). Functional optimality underpins the repeated evolution of the
418 extreme saber-tooth morphology. Curr. Biol. *35*, 455-467.e6.
419 10.1016/j.cub.2024.11.059.

420 47. Rose, K.D. (1981). Composition and species diversity in Paleocene and Eocene
421 mammal assemblages: an empirical study. J. Vertebr. Paleontol. *1*, 367–388.
422 10.1080/02724634.1981.10011907.

423 48. Hooker, J.J. (2000). Paleogene mammals: crises and ecological change. Biot.
424 response to Glob. Chang. last *145*, 333–349.

425 49. Beard, K.C. (1998). East of Eden: Asia as an important center of taxonomic
426 origination in mammalian evolution. Bull. Carnegie Museum Nat. Hist. *34*, 5–39.

427 50. Maas, M.C., Krause, D.W., and Strait, S.G. (1988). The decline and extinction of
428 Plesiadapiformes (Mammalia:? Primates) in North America: displacement or
429 replacement? Paleobiology *14*, 410–431.

51. Lopatin, A. V (2006). Early Paleogene insectivore mammals of Asia and establishment of the major groups of Insectivora. Paleontol. J. *40*, S205–S405. 10.1134/S0031030106090012.

52. Culver, S.J., and Rawson, P.F. (2006). Biotic response to global change: the last 145 million years (Cambridge University Press).

53. Beard, C. (2002). East of Eden at the Paleocene/Eocene boundary. Science . *295*, 2028–2029.

54. Feijó, A., Ge, D., Wen, Z., Cheng, J., Xia, L., Patterson, B.D., and Yang, Q. (2022). Mammalian diversification bursts and biotic turnovers are synchronous with Cenozoic geoclimatic events in Asia. Proc. Natl. Acad. Sci. *119*, e2207845119. 10.1073/pnas.2207845119.

55. McKenna, M.C., Chow, M., Ting, S., and Luo, Z. (1989). Radinskya yupingae a perissodactyl-like mammal from the Late Paleocene of China. In The evolution of perissodactyls, pp. 24–36.

56. Goswami, A., Binder, W.J., Meachen, J., and O'Keefe, F.R. (2015). The fossil record of phenotypic integration and modularity: A deep-time perspective on developmental and evolutionary dynamics. Proc. Natl. Acad. Sci. *112*, 4891–4896. 10.1073/pnas.1403667112.

57. Peppe, D.J. (2010). Megafloral change in the early and middle Paleocene in the Williston Basin, North Dakota, USA. Palaeogeogr. Palaeoclimatol. Palaeoecol. *298*, 224–234.

58. Scheffers, B.R., De Meester, L., Bridge, T.C.L., Hoffmann, A.A., Pandolfi, J.M., Corlett, R.T., Butchart, S.H.M., Pearce-Kelly, P., Kovacs, K.M., Dudgeon, D., et al. (2016). The broad footprint of climate change from genes to biomes to people. Science . *354*, aaf7671. 10.1126/science.aaf7671.

59. Tseng, Z.J., Garcia-Lara, S., Flynn, J.J., Holmes, E., Rowe, T.B., and Dickson, B. V (2023). A switch in jaw form–function coupling during the evolution of mammals. Philos. Trans. R. Soc. B Biol. Sci. *378*, 20220091. 10.1098/rstb.2022.0091.

60. Schultz, J.A. (2025). A perspective from the Mesozoic: Evolutionary changes of the mammalian skull and their influence on feeding efficiency and high-frequency hearing. Anat. Rec., 1–16. https://doi.org/10.1002/ar.25652.

61. Zachos, J., Pagani, M., Sloan, L., Thomas, E., and Billups, K. (2001). Trends, rhythms, and aberrations in global climate 65 Ma to present. Science . *292*, 686–693.

62. Speijer, R.P., Pälike, H., Hollis, C.J., Hooker, J.J., and Ogg, J.G. (2020). The Paleogene Period (Chapter 28). In Geological Time Scale, F. M. Gradstein, J. G. Ogg, M. D. Schmitz, and G. M. Ogg, eds. (Elsevier), pp. 1087–1140.

63. Cande, S.C., and Kent, D. V (1995). Revised calibration of the geomagnetic polarity timescale for the Late Cretaceous and Cenozoic. J. Geophys. Res. Solid Earth *100*, 6093–6095.

64. Pampush, J.D., Winchester, J.M., Morse, P.E., Vining, A.Q., Boyer, D.M., and Kay, R.F. (2016). Introducing molaR: a New R Package for Quantitative Topographic Analysis of Teeth (and Other Topographic Surfaces). J. Mamm. Evol. *23*, 397–412. 10.1007/s10914-016-9326-0.

65. Bunn, J.M., Boyer, D.M., Lipman, Y., St. Clair, E.M., Jernvall, J., and Daubechies, I. (2011). Comparing Dirichlet normal surface energy of tooth crowns, a new technique of molar shape quantification for dietary inference, with previous methods in isolation and in combination. Am. J. Phys. Anthropol. *145*, 247–261.

66. Waldman, E., Gonzalez, Y., Flynn, J.J., and Tseng, Z.J. (2023). Dental topographic proxies for ecological characteristics in carnivoran mammals. J. Anat. *242*, 627–641. https://doi.org/10.1111/joa.13806.

67. Berthaume, M.A., Lazzari, V., and Guy, F. (2020). The landscape of tooth shape: Over 20 years of dental topography in primates. Evol. Anthropol. Issues, News, Rev. *29*, 245–262.

68. Evans, A.R., Wilson, G.P., Fortelius, M., and Jernvall, J. (2007). High-level similarity of dentitions in carnivorans and rodents. Nature *445*, 78–81.

486 69. DeMers, A.C., and Hunter, J.P. (2024). Dental complexity and diet in amniotes: A
487 meta-analysis. PLoS One *19*, e0292358.

488 70. Crofts, S.B., Smith, S.M., and Anderson, P.S.L. (2020). Beyond Description: The
489 Many Facets of Dental Biomechanics. Integr. Comp. Biol. *60*, 594–607.
490 10.1093/icb/icaa103.

491 71. Crompton, A.W., and Hiiemae, K. (1969). How mammalian molar teeth work.
492 Discovery *5*, 23–34.

493 72. Bhullar, B.-A.S., Manafzadeh, A.R., Miyamae, J.A., Hoffman, E.A., Brainerd, E.L.,
494 Musinsky, C., and Crompton, A.W. (2019). Rolling of the jaw is essential for
495 mammalian chewing and tribosphenic molar function. Nature *566*, 528–532.
496 10.1038/s41586-019-0940-x.

497 73. Simpson, J.J. (1936). Studies of the earliest mammalian dentitions. Dent. Cosm.
498 *78*, 791–800.

499 74. Yamanaka, A., Haider, Y., Morita, W., Corfe, I., Nakamura, N., and Goto, T.
500 (2024). Developmental process of the modern house shrew's molars: implications
501 for the evolution of the tribosphenic molar in Mesozoic mammals. Evolution (N.
502 Y). *78*, 463–479. 10.1093/evolut/qpad228.

503 75. Lucas, P.W., and van Casteren, A. (2014). The Wear and Tear of Teeth. Med.
504 Princ. Pract. *24*, 3–13. 10.1159/000367976.

505 76. van Casteren, A., and Crofts, S.B. (2019). The Materials of Mastication: Material
506 Science of the Humble Tooth. Integr. Comp. Biol. *59*, 1681–1689.
507 10.1093/icb/icz129.

508 77. Crofts, S. (2015). Finite element modeling of occlusal variation in durophagous
509 tooth systems. J. Exp. Biol. *218*, 2705–2711. 10.1242/jeb.120097.

510 78. Pérez-Ramos, A., Romero, A., Rodriguez, E., and Figueirido, B. (2020). Three-
511 dimensional dental topography and feeding ecology in the extinct cave bear. Biol.
512 Lett. *16*, 20200792. 10.1098/rsbl.2020.0792.

513 79. Pollock, T.I., Panagiotopoulou, O., Hocking, D.P., and Evans, A.R. (2022). Taking
514 a stab at modelling canine tooth biomechanics in mammalian carnivores with
515 beam theory and finite-element analysis. R. Soc. Open Sci. *9*, 220701.
516 10.1098/rsos.220701.

517 80. Villalobos-Chaves, D., and Santana, S.E. (2022). Craniodental traits predict
518 feeding performance and dietary hardness in a community of Neotropical free-
519 tailed bats (Chiroptera: Molossidae). Funct. Ecol. *36*, 1690–1699.
520 https://doi.org/10.1111/1365-2435.14063.

521 81. Sender, R.S., and Strait, D.S. (2023). The biomechanics of tooth strength: testing
522 the utility of simple models for predicting fracture in geometrically complex teeth.
523 J. R. Soc. Interface *20*, 20230195. 10.1098/rsif.2023.0195.

524 82. Berthaume, M.A. (2016). On the Relationship Between Tooth Shape and
525 Masticatory Efficiency: A Finite Element Study. Anat. Rec. *299*, 679–687.
526 https://doi.org/10.1002/ar.23328.

527 83. Ungar, P.S. (2015). Mammalian dental function and wear: A review. Biosurface
528 and Biotribology *1*, 25–41. https://doi.org/10.1016/j.bsbt.2014.12.001.

529 84. Dumont, E.R. (1995). Enamel Thickness and Dietary Adaptation among Extant
530 Primates and Chiropterans. J. Mammal. *76*, 1127–1136. 10.2307/1382604.

531 85. Shellis, R.P., Beynon, A.D., Reid, D.J., and Hiiemae, K.M. (1998). Variations in
532 molar enamel thickness among primates. J. Hum. Evol. *35*, 507–522.

533 86. Dumont, E.R., Grosse, I.R., and Slater, G.J. (2009). Requirements for comparing
534 the performance of finite element models of biological structures. J. Theor. Biol.
535 *256*, 96–103. 10.1016/j.jtbi.2008.08.017.

536 87. He, L.H., Fujisawa, N., and Swain, M. V (2006). Elastic modulus and stress–strain
537 response of human enamel by nano-indentation. Biomaterials *27*, 4388–4398.
538 https://doi.org/10.1016/j.biomaterials.2006.03.045.

539 88. Conith, A.J., Imburgia, M.J., Crosby, A.J., and Dumont, E.R. (2016). The
540 functional significance of morphological changes in the dentitions of early

mammals. J. R. Soc. Interface *13*, 20160713. 10.1098/rsif.2016.0713.

89. Lee, J.J.-W., Constantino, P.J., Lucas, P.W., and Lawn, B.R. (2011). Fracture in teeth—a diagnostic for inferring bite force and tooth function. Biol. Rev. *86*, 959–974. https://doi.org/10.1111/j.1469-185X.2011.00181.x.

90. Irschick, D.J., Meyers, J.J., Husak, J.F., and Le Galliard, J.-F. (2008). How does selection operate on whole-organism functional performance capacities? A review and synthesis. Evol. Ecol. Res. *10*, 177–196.

91. Team, R.C. (2025). R: A Language and Environment for Statistical Computing.

92. Adams, D.C., and Otárola-Castillo, E. (2013). geomorph: an r package for the collection and analysis of geometric morphometric shape data. Methods Ecol. Evol. *4*, 393–399. https://doi.org/10.1111/2041-210X.12035.

93. Klingenberg, C.P. (2014). Studying morphological integration and modularity at multiple levels: concepts and analysis. Philos. Trans. R. Soc. B Biol. Sci. *369*, 20130249. 10.1098/rstb.2013.0249.

Acknowledgments:

We thank I. Ruiz for assisting with generating 3D tooth models from CT data; X. Tseng for assisting with data collection; P. Holroyd for assisting with locating specimen casts in the collections of the University of California Museum of Paleontology; J. Liu for helpful discussion and comments on earlier versions of the study. Z. Luo provided earnest and constructive feedback on an earlier version of the study. Editor S. Rasmann and two anonymous reviewers provided highly constructive feedback on the study.

Funding: This study was funded in part by grant 213109 from the Nanjing Institute of Geology and Paleontology, Chinese Academy of Sciences (to QL and ZJT) and National Key Research and Development Project of China (2024YFF0807603; to QL).

Author contributions:

Conceptualization: All authors.

Methodology: ZJT.

Formal analyses: ZJT.

Investigation: All authors.

Results acquisition: ZJT.

Raw data acquisition (surface and CT scan data): ZJT, QL.

Writing, original draft: ZJT.

Writing, review, and editing: All authors.

Visualization: ZJT, QL.

Competing interests: The authors declare that they have no competing interests.

Resource availability:

- Requests for further information and resources should be directed to and will be fulfilled by the lead contact, Jack Tseng (zjt@berkeley.edu).
- Code associated with analyses is included with this article.
- Raw data are available in the supplementary materials.
- All original fossil specimens are accessioned in the Institute of Vertebrate Paleontology and Paleoanthropology, Chinese Academy of Sciences.

Supplemental information

Document S1. Figures S1–S11, Tables S1–S3, and supplemental references

Data S1

Data S2

Data S3

Data S4

Data S5

Data S6

Data S7

Data S8

Data S9

Data S10

Figure Legends

Fig. 1. Temperature and fossil mammal dental trait shifts during the first 10 Myr of the Cenozoic. (A) Dental topographic trait values (boxplots) and mean variance (red curves) during the first 10 Myr of the Cenozoic, signifying the time after the K-Pg mass extinctions and before the Paleocene-Eocene hyperthermal event. Global temperature curve based on Zachos et al. [61]. Dental traits measured include crown complexity (OPCR, orientation patch count rotated), curvature (DNE, Dirichlet normal energy), height (RFI, relief index), and slope. (B) Mammal tooth size distributions represented by log 10 square root tooth area, in units of log10 millimeters. (C) Variance of compressive bite performance based on tooth crown finite element simulations, in units of squared Joules. (D) Variance of shear bite performance based on tooth crown finite element simulations, in units of squared Joules. Examples of endemic Asian fossil specimens analyzed: (E) Lateral and ventral views of early Paleocene Chinese endemic pantodont (CEP) *Bemalambda nanhsiungensis* IVPP (Institute of Vertebrate Paleontology and Paleoanthropology, Chinese Academy of Sciences) V4116. (F) Lateral and ventral views of middle Paleocene CEP *Harpyodus decorus* IVPP 5035.1. (G) Lateral and occlusal views of late Paleocene CEP *Guichilambda zhaii* IVPP V12037.2 (dentary) and V12037.3 (maxillary fragment). Firey asteroid symbols indicate the end-Cretaceous asteroid impact in the Yucatán Peninsula; thermometer symbols indicate the Paleocene-Eocene hyperthermal event. Subdivisions of the Paleocene approximately correspond to the Shanghuan, Nongshanian, and Gashatan Asian Land Mammal Ages, respectively (see supplemental text for competing age boundary scenarios).

Fig. 2. Association of paleopalynological data from the Nanxiong Basin, south China, and late Paleocene niche expansion in endemic Asian fossil mammals. (A) Proportion of environmental humidity indicator taxa from early versus late Paleocene paleobotanical localities, respectively, in the Nanxiong Basin; data based on [35,36](Data S12). (B) Boxplots of dental complexity (OPCR, orientation patch count rotated) in the Chinese endemic pantodont (CEP) data partition across the three Paleocene time intervals examined. Note the concomitant increase in CEP tooth complexity (OPCR) and increased proportion of drought-tolerant plant species in the Nanxiong Basin during the late Paleocene. (C) Principal component morphospace of all tooth data analyzed; convex

hulls delineate overall morphospace occupation during each time interval. Eigenvectors of the four dental topographic traits are indicated in blue. Late Paleocene shift and expansion in dental topographic morphospace is statistically significant at the $p = 0.05$ level (Table 1). Pantodont silhouette by S. Traver from phylopic.org.

Fig. 3. Correlation plots of dental topographic and bite performance traits in endemic Asian Paleocene mammals. (A) Hypothetical correlation scenarios used to interpret stasis, directional, verses decoupled change through time in specimen data. (B) Pairwise ranked correlation coefficient estimated using Kendall's τ between early and middle Paleocene dental topographic and performance traits in the main dataset. (C) Correlation between middle and late Paleocene traits in the main dataset. (D) Correlation between early and middle Paleocene traits in the Chines endemic pantodont (CEP) data partition. (E) Correlation between middle and late Paleocene traits in the CEP data partition. Topography-performance correlations are marked in red boxes. Decoupled/reversed trait correlations are marked in gray boxes.

All data	Early-Middle Paleocene	Middle-Late Paleocene
DNE	0.7753	**0.003**
OPCR	0.0902	**0.0001**
RFI	0.605	**0.0128**
Slope	0.643	0.287
PCA Disparity	0.4562	**0.0001**
Tooth size	**<0.0001**	**<0.0001**
Chinese Endemic Pantodonts		
DNE	0.9264	**0.0002**
OPCR	0.17	**<0.0001**
RFI	1	1
Slope	1	1
Chinese Arctostylopids and Anagalids		
DNE	0.847	0.135
OPCR	0.47	0.18
RFI	0.2486	**0.0056**
Slope	0.642	0.269

Table 1. Pairwise t test of dental topographic trait and disparity differences across adjacent time bins. Dental topographic trait differences are assessed across time intervals in all-data, Chinese endemic pantodont, and non-pantodont partitions. Dental trait disparity was estimated based on all principal component axes using the outputs of PCA. Tooth size variance differences were calculated from tooth area or square root of tooth area in all-data and no-outlier partitions to assess effect of outliers on statistical significance (see Data S6 for details). Bolded font indicates *p* values < 0.05.

656 **METHOD DETAILS**

657 We focused sampling on three clades: Chinese endemic Pantodonta, Chinese
658 Arctostylopida, and Anagalida. Additional data were collected on other clades (e.g.,
659 Chinese Tillodontia) opportunistically when well-preserved specimens were available
660 (Data S1). These three main clades together represent >50% of the species found in
661 Paleocene faunas across China [11]. They also individually represent the most diverse
662 clades across the three Asian Land Mammal Ages of the Paleocene: Shanghuan,
663 Nongshanian, and Gashatan. By contrast, these clades are reduced to <25% of species
664 diversity in Eocene assemblages in China, finally disappearing altogether in the late
665 Oligocene. Therefore, we take the three clades to be representative of mammal
666 assemblage dynamics during the Paleocene time interval in China.

667 Historically, Paleocene fossil mammal faunas in China have been defined based
668 on biostratigraphic criteria and supplemented by magnetostratigraphic correlations where
669 available. Here we follow the assessment of [62] in generally correlating the Shanghuan
670 Asian Land Mammal Age (ALMA) with the Puercan and Torrejonian North American Land
671 Mammal Ages (NALMAs), the Nongshanian ALMA with early to middle Tiffanian NALMAs,
672 and the Gashantan ALMA with late Tiffanian and Clarkforkian NALMAs, respectively (see
673 [11] for an alternative interpretation). Additionally, the Shanghuan and Nongshanian
674 boundary was interpreted by [25] to be at the top of Chron C27N, which is dated at 60.920
675 Myr ago in the Geomagnetic Polarity Time Scale [63] but indicated as closer to ~62.3 Myr
676 ago in [62]. Similarly, the Nongshanian-Gashatan boundary has been variably defined at
677 59.24 Myr ago [62] or the base of Chron C26N, which is 57.911 Myr ago [63]. In contrast, the
678 end of the Gashatan coincides with the Paleocene-Eocene boundary at 56 Myr ago and
679 has been consistently defined as such [62]. Given these existing uncertainties, we use the
680 terms ‘early Paleocene’, ‘middle Paleocene’, and ‘late Paleocene’ to refer generally to the
681 Shanghuan, Nongshanian, and Gashatan ALMAs, respectively, in this study.

682 We analyzed 200 individual teeth from 48 specimens, representing 37 species
683 (Data S1-S2). The teeth represent 2 upper first premolars, 4 upper second premolars, 15
684 upper third premolars, 19 upper fourth premolars, 22 upper first molars, 23 upper second
685 molars, 16 upper third molars, 3 lower first premolars, 5 lower second premolars, 13 lower
686 third premolars, 17 lower fourth premolars, 20 lower first molars, 22 lower second molars,

687 and 19 lower third molars. These tooth positions were selected from a broader
688 examination of ~300 individual teeth from 72 specimens. We vetted the specimens and
689 excluded 99 tooth positions (~33% of teeth initially chosen for possible inclusion) from our
690 analyses because they either (1) were partially or completely broken at the crown, (2)
691 were in an advanced stage of attritional wear where no cusps could be identified, or (3)
692 possessed a combination of the two aforementioned conditions. The assigned geologic
693 age of the studied specimens spans the entire Paleocene, binned into early (n = 91 teeth),
694 middle (n = 46 teeth), and late Paleocene (n = 63 teeth) data partitions. To maximize
695 sample size while minimizing disturbance to more delicate specimens, a combination of
696 original specimens and previously produced high-fidelity specimen casts were used in
697 our sampling of dental crown morphology.

698 Given the rarity of Paleocene fossil material from China, we combined data from
699 different tooth positions into three pooled samples, one for each of the time intervals
700 examined (early, middle, late Paleocene). We treated the pooled samples as
701 representative of the range of dental topographic features and bite performance traits
702 available to the mammal taxa under study. In this way, the variance estimates are
703 interpreted as measures of the morphological and performance heterogeneity present in
704 each time interval dataset. To further tease out the possibility of specific tooth positions
705 driving the overall trends observed in the pooled samples, we also performed the DTA,
706 FEA, DTA-FEA correlation, and tooth size through-time analyses using per-tooth data
707 partitions.

708

709 Tooth shape estimates using Dental Topographic Analysis

710 We digitized dental crown morphology via microCT either using a GE v|tome|x m
711 300/180 kV micro-computed-tomography system (GE Measurement & Control Solutions,
712 Wuntsdorf, Germany), housed at the Institute of Vertebrate Paleontology and
713 Paleoanthropology (IVPP), Chinese Academy of Sciences (CAS), or a GE Phoenix
714 Nanotom M in the Functional Anatomy and Vertebrate Evolution Laboratory, University of
715 California, Berkeley. Projection images (1,000 to 1,500 images depending on specimen
716 size) were acquired with an isotropic voxel size of 10 to 40 μm, at an energy range of
717 120-150 kV, current of 100-150 μA. Additionally, surface 3D scans (generated using

718 IVPP's Artec Space Spider 3D scanner, with a precision of 0.05 mm and resolution of 0.1
719 mm) were used for larger specimens to efficiently obtain surface morphology data. The
720 enamel caps (the crown portion of each tooth above the enamel-dentine junction) were
721 extracted from the specimen models using Geomagic Wrap v2021; all crown surface
722 holes (generated from scanning imperfections or digitally removed sediment) were
723 patched, the models were remeshed with triangles that have aspect ratios (base:height
724 or edge-edge) of <10 and decimated to ~10,000 triangles. Finally, we standardized the
725 spatial orientation of all tooth crowns before exporting them as .ply files for dental
726 topographic analysis (DTA). Individual tooth crown (enamel cap) models have the Z axis
727 normal to the occlusal plane, the X axis parallel to the mesial-distal axis, and the Y axis
728 parallel to the labial-lingual axis.

729 Exported meshes were further vetted and prepared for DTA within the R
730 programming environment. We used functions implemented in the *molaR* R package [64]
731 for all of the steps described next. First, all .ply files are further cleaned using
732 'molarR_Clean' to remove floating points/vertices and any triangular faces with zero area.
733 Then, the batch function 'molarR_Batch' was used to calculate four dental topographic
734 metrics: DNE, OPCR, Slope, and RFI.

735 Dirichlet Normal Energy (DNE) is a measure of occlusal sharpness, using a
736 quantification of surface energy in tooth crowns relative to a gently curving or flat mesh
737 surface. Steep, high, and/or shearing cusps tend to produce higher DNE values in DTA,
738 whereas bulbous cusps tend to produce lower DNE values [65,66]. DNE has been used to
739 successfully distinguish folivores, omnivores, and frugivores in euarchontan (primates,
740 colugos, tree shrews) mammals [65,67].

741 Orientation Patch Count Rotated (OPCR) is a measure of tooth crown complexity,
742 using quantification of distinct patches on the crown face that possess unique orientations.
743 Teeth with larger number of cusps and crenulations tend to produce higher OPCR values,
744 whereas teeth with fewer cusps and simpler ridges tend to produce lower OPCR values.
745 This metric has been used effectively to distinguish convergently evolved carnivore
746 versus herbivore species across multiple mammalian orders [68]. DeMers and Hunter [69]
747 suggest that OPCR does not currently provide a reliable approximation for the degree of
748 adaptation to herbivory, and that any interpretation of ecomorphological differences

749 should be made within a taxon-specific context. Given the narrow set of clades targeted
750 in our dataset, we interpret increasing OPCR as an indication of increased functional
751 capability to process vegetation. A related measure, slope, quantifies the mean tilt of the
752 tooth surface relative to the occlusal plane. Teeth with lower and more gently curving
753 cusps tend to have lower slopes, whereas teeth with sharp and/or abruptly ridged crests
754 tend to have higher slopes.

755 Relief Index (RFI) is a measure of the relative height and complexity of the tooth
756 crown, using the values of the 3D surface and 2D 'footprint' areas of the tooth crown.
757 RFI has been shown to be effective in distinguishing frugivores from insect and leaf
758 specialists in euarchontan mammals [65]. Furthermore, RFI is also able to distinguish
759 carnivoran species at different trophic levels and dietary breadths [66].

760 Overall, we use these DTA traits as indicators of ecomorphological capacity, but
761 do not link them explicitly to dietary categories. The craniodental morphology of archaic
762 placental clades in general have not been demonstrated to share the same structure-
763 function linkages as crown mammals, so aforementioned linkages between DTA and
764 dietary ecology from studies of extant species only serve as evidence that DTA is a
765 potentially useful ecomorphological proxy. We do not directly apply those DTA-diet
766 relationships to the Paleocene fossil mammal dataset.

767 All tooth crown models are provided as ply files and deposited in FigShare
768 (10.6084/m9.figshare.28611854).

769

770 <u>Tooth performance estimates using Finite Element Analysis</u>

771 The common inference that dental morphology can reflect dietary adaptations
772 makes an underlying connection between the two traits through biomechanical
773 performance; the mechanical performance imbued by a particular morphological
774 configuration accomplishes one or more food acquisition and/or processing tasks. Such
775 mechanical performance links can be tested using experimental and simulation
776 approaches on both theoretical grounds and actual tooth shapes [70]. Here we applied a
777 simulation approach to estimate two general performance traits commonly interpreted for
778 mammalian tribosphenic teeth: puncturing/compressing and shearing/grinding [71]. The
779 ancestral therian tribosphenic stroke, or the chewing movement underlying mammals with

780 unfused mandibular symphysis and tribosphenic molars, has been reconstructed to
781 involve significant components of (1) long-axis rotation in each hemimandible and (2)
782 mortar-and-pestle grinding between upper and lower cusps [72]. These movements are
783 associated with the 'lock-and-key' occlusion of a stereotypical mammalian tribosphenic
784 dentition, which exhibit tall crest-like cusps in the trigonid and lower basin-like valleys in
785 the talonid of lower molars that articulate with their corresponding upper teeth (Fig. S3).

786 We used finite element analysis (FEA) to estimate the work efficiency of different
787 tooth crowns subjected to compressive/puncturing and shearing/grinding forces, the two
788 major masticatory actions of tribosphenic teeth [71,73,74]. Adequate compressive and
789 puncturing forces applied through individual or combined action of cusps are needed to
790 overcome the fracture strength of brittle and tough food such as seeds and invertebrate
791 exoskeletons in order for individuals to access soft and/or more nutritious tissues within.
792 Sufficient shearing and grinding forces applied through surfaces or cusp edges are
793 necessary to further break down food boli into smaller pieces to aid in the digestive
794 process. The combination of these two major functions of tribosphenic teeth is thought to
795 be a foundational adaptation that enabled the mammalian radiation [71,72,75]. We focused
796 on the dental enamel portion of the tooth crown in our biting simulations because it is the
797 most mineralized vertebrate tissue and typically the best-preserved component of fossil
798 teeth. The fracture mechanics of mammalian dental enamel is thought to be intimately
799 related to dietary function [76], including the evolution of different enamel thickness in
800 different feeding ecomorphologies [28]. It is important to note that because the dental data
801 available for this study included not only CT scans, but also surface scans and specimen
802 casts, enamel thickness was not quantifiable for most specimens in our dataset (see
803 below for a description of enamel thickness scaling procedure applied in the simulations).

804 The two masticatory scenarios tested, compressing/puncturing versus
805 shearing/grinding, have previously been shown to be broadly connected to tooth topology.
806 Taller cusps (approximated in our study by Relief Index and partially by Slope) and more
807 convex crowns (approximated in our study by DNE) tend to exhibit higher strain in finite
808 element models of hypothetical tooth shapes [77]. However, there is by no means a
809 consensus on the presence of a tight form-function linkage across all tooth types and/or
810 clades. Whereas a dental topography to food mechanical property linkage can be

811 detected in some extant carnivores [78,79], bats [80], and primate-like tooth models [81], a form-
812 function relationship between dental topography and tooth/food mechanical properties is
813 absent in other model systems [67,82]. Therefore, we incorporated biomechanical
814 simulations as an explicit test of the mechanical performance associations implied by the
815 DTA-flora correlations established in the dental topography and paleoenvironmental
816 portion of our analyses. The main question addressed by these simulations is not
817 necessarily whether a form-function linkage exists in the Paleocene mammal dataset, but
818 whether there is a consistent relationship between DTA and FEA traits across the three
819 time bins of the Paleocene. If such consistent linkages are observed, it would suggest a
820 stasis in dental topography and compressive/shearing performance through the first 10
821 million years of the Cenozoic in our dataset; alternatively, any significant changes in the
822 topography-performance relationship would indicate substantial evolutionary change
823 through the same time period.

824 We imported the same tooth crown models generated for DTA into the Strand7
825 finite element software (Strand7 Pty Ltd, Australia) to create finite element models of the
826 individual teeth. The tooth meshes are composed of two-dimensional, three-noded
827 triangular elements ranging between 9,000-10,000 elements, with assigned thickness
828 parameter (see below) so they behave similarly to single-layer 3-D elements. A
829 convergence test was done on two of the specimens (IVPP V5228, V5231) and indicated
830 that the <10,000 three-noded triangular plate elements (tri3) returned simulation output
831 values with less than 10% deviation from higher resolution meshes of the same models
832 (Fig. S3). Therefore, we deemed the default resolution of the tooth meshes used in DTA
833 to be sufficient for finite element simulations. Furthermore, because the dataset contained
834 digital models built from both CT and surface scan data, not all specimens have enamel
835 thickness information. Although increased enamel thickness has been associated with
836 durophagy in mammals, there appears to be taxon-specific patterns of enamel thickness
837 to tooth size and dietary ecology, in addition to extensive variation in intra-tooth enamel
838 thickness distributions [83–85]. In absence of information on enamel thickness differences
839 among the taxa studied, we standardized the thickness of the tooth crown models
840 isometrically to be 10% of the total surface area of a given tooth model. As such, the
841 simulation results should be treated as enamel cap shape-derived performance traits,

842 rather than those based on a fully parameterized enamel model incorporating localized
843 thickness and inter-specific allometric differences.

844 We scaled applied forces on the teeth, simulating compressive or shearing loads,
845 to be a value equivalent to total model surface area (but in units of Newtons instead of
846 mm^2). Compressive loads were represented on each tooth by a single nodal force vector
847 directed towards the base of the crown along the height axis of each tooth, on the tallest
848 cusp or cuspid (which is typically the protocone for upper molars and protoconid for lower
849 molars, or the main cusp in premolars). This configuration simulated a compressive load
850 directed into the tallest cusp (towards the root) on a given tooth from a food item (Fig S3),
851 as reconstructed for the mammalian tribosphenic bite during a crushing or puncturing
852 movement [71,72]. Shearing loads were represented on each tooth by two nodal force
853 vectors, one on each of the two tallest cusps or cuspids; the two nodal forces are of equal
854 magnitude but opposing directions, perpendicular to the long axis of the tooth and in the
855 occlusal plane. This configuration portrays a shearing motion along the short axis of the
856 tooth (Fig. S3), and simulates tooth-to-tooth and tooth-to-food contact during the 'mortar
857 and pestle' grinding rotation movement reconstructed for the ancestral mammal
858 tribosphenic bite [72]. This force magnitude standardization procedure effectively generates
859 identical force to area ratios across the models, ensuring that the magnitudes of
860 mechanical stress placed on the model are the same across models of different sizes;
861 furthermore, we adjusted the strain energy values collected for each tooth model
862 simulation using the volume and input force ratio-based correction equation provided in
863 [86]. Given our objective to assess the association between relative performance traits and
864 DTA metrics, with the latter being size-free variables, only the relative magnitudes of bite
865 performance, rather than absolute values, were collected from the performance analyses.

866 After each tooth crown model was defined using the criteria outlined above,
867 homogenous material properties were assigned. All models were defined as plate models
868 (with thickness scaled to surface area) with a Young's (elastic) modulus of 80 GPa [87] and
869 Poisson Ratio of 0.3. Next, each tooth was constrained from translation and rotation using
870 four nodal constraints distributed in the four corners of each tooth, respectively (Fig. S3).

871 All bite scenarios were solved using the linear static solver implemented in Strand7.
872 A total number of 400 analyses were performed (one compressive bite and one shearing

873 bite simulation for each of the 200 tooth specimens in the dataset). We extracted two
874 traits from the models: compressive bite strain energy and shear bite strain energy. Strain
875 energy is defined as the area under a stress-strain curve of an object under load;
876 operationally it measures the amount of work done by the load to deform the object
877 (analogous to experimental work-to-fracture measurements)[88]. An object that is more
878 resistant to deformation would have lower strain energy than an object that easily deforms
879 under load. The use of work-to-fracture measures to assess tooth performance is
880 consistent with the understanding of mammalian tooth enamel as a fracture-prone, yet
881 fracture-resistant, biological tissue [89]. In such a framework, fracture resistance is
882 expected to be directly related to the amount of force an individual is able to exert through
883 the tooth crown during mastication, and by extension the hardest or toughest food item
884 that can be processed without catastrophic damage to the tooth crown itself. Fracture
885 resistance (as approximated by strain energy in this study) is also likely to be a stronger
886 target of selection in mammals compared to those of other toothed vertebrates, given the
887 former's diphyodonty (having only two sets of tooth instead of continuous dental
888 replacement) and thus necessity to prolong usable tooth lifespan[83]. Therefore, we used
889 strain energy values under compressive and shear bite simulation scenarios as a proxy
890 for the effectiveness of each tooth crown model at resisting deformation from the
891 respective biting forces. A tooth that is more resistant (i.e., have lower strain energy
892 values) from compressive forces would be able to more effectively crush/puncture harder
893 food items, and a tooth more resistant from shear forces would be able to cut/grind
894 tougher food items. We modify Irschick et al.'s[90] definition of whole-organism performance
895 and define bite performance in the context of this study as the capacity of individual tooth
896 models to resist simulated compressive and shearing forces, which represent ecologically
897 relevant factors that influence masticatory efficacy.
898 All finite element models are provided as NASTRAN/text files and deposited in
899 FigShare (10.6084/m9.figshare.28611854).
900
901 <u>Sensitivity validation of original versus cast specimen models</u>
902 The tooth dataset developed in this study contains a mixture of CT scans of original
903 and casts of fossil specimens. In order to assess the potential discrepancies in DTA and

904 FEA trait values collected from cast versus original specimen derived models, either due
905 to phenotypic details not captured in cast specimens or deterioration of epoxy or resin-
906 based casts over time, we randomly sampled two specimens for which both original and
907 cast based models were analyzed. Results from DTA and FEA of the CT-derived models
908 of lower first molars from IVPP V5228 (*Altilambda pactus*) and V5231 (*A. tenuis*) were
909 compared to those conducted on digital models built from CT scans of casts of those
910 specimens.

911 We used the 'n-point' and 'global' alignment functions in Geomagic Wrap to first
912 align the models using arbitrary homologous landmarks visually identified on both tooth
913 models and then the automatic global alignment function to maximize overlap between
914 the two models in 3D coordinate space. The 'deviation' function in Geomagic Wrap was
915 then used to calculate summary statistics for linear deviations orthogonal to the surface
916 of the original model. The V5228 Lm1 model showed a maximum deviation of 0.58 mm
917 (5.8% of crown height) and average deviation of 0.04-0.09 mm (<1% of crown height),
918 with a standard deviation of 0.11 mm (1% of crown height). The V5231 Lm1 model
919 showed a maximum deviation of 0.38 mm (6% of crown height) and average of 0.03-0.04
920 mm (<1% of crown height), with a standard deviation of 0.06 mm (1% of crown height)(Fig.
921 S3).

922

923 <u>Quantification of uncertainty ranges for bootstrap sampling</u>

924 We then subjected the cast-based models to DTA and FEA. In both cases, the DTA
925 values between cast and specimen models are the most different for DNE (30-40%
926 difference), followed by OPCR (18-32% difference), then RFI (2-13% difference), and
927 finally Slope (1-5% difference) (Data S4). Also in both cases, adjusted compressive SE
928 values differed by 14-41% and adjusted shear values differed by 20% (Data S3). Based
929 on these specimen-cast validation tests, we set a conservative +/- 40% uncertainty range
930 for all DTA and FEA values obtained from all cast-based tooth models. DTA and FEA trait
931 mean and variance estimates used for downstream statistical analyses were then
932 calculated using a bootstrap sampling scheme where 1,000 replicates of the DTA and
933 FEA datasets were passed through the statistical tests (see Quantification and statistical
934 analysis section, below). Overall, the early and middle Paleocene time bins contain

935 around 50% cast data, whereas the late Paleocene time bin contains 66% cast data. If
936 data uncertainty from original versus specimen models present a major signal, we would
937 expect the late Paleocene time interval to always show higher variance given an
938 abundance of cast data in that time bin. We did not observe any consistent trends of high
939 variance in the late Paleocene in the 1,000 bootstrap samples, suggesting that the results
940 are not significantly biased by data quality differences between cast and original
941 specimen derived models (Fig. S4).
942
943 Time bin duration correction and tooth position ratios
944 According to Ni et al. [6], the Shanghuan Asian Land Mammal Age (ALMA) faunas
945 in Guangdong and Anhui range from 66-61.6 Ma (or 4.4 Myr in duration), the
946 Nongshanian ALMA faunas in Guangdong, Jiangxi, and Anhui range from 61.6-59.2 Ma
947 (or 2.4 Myr in duration), and the Gashatan ALMA faunas in Anhui range from 59.2 to 56
948 Ma (or 3.2 Myr in duration). Given the different durations represented in each of the three
949 time bins used in our analyses, we corrected all variance estimates by dividing the
950 variance calculated in each of the bootstrapped samples by the time duration of the
951 respective time bin. In this manner, the variance values reported in the study represent
952 per-million-year values.
953 We used pie chart analysis to verify that the proportions of tooth positions in each
954 time bin are not substantially different from each other (Fig. S1). However, we caution that
955 time bin comparisons of individual tooth positions are unlikely to be statistically robust
956 because of small sample sizes. We only use aggregates of dental positions (all teeth,
957 molars, or premolars) in our data partition analyses and interpretation.
958
959 **QUANTIFICATION AND STATISTICAL ANALYSIS**
960 We used the following features of the dental topography and performance data as
961 the basis for assessing faunal assemblage trait shifts through the Paleocene: trait mean,
962 variance, trait-to-trait correlation, and partition-to-partition correlation. We used ANOVA
963 (Analysis of Variance) and pairwise t test to compare trait means, F test to compare trait
964 variance, linear regression analysis and Kendall's τ to compare trait-to-trait correlation,
965 and two-block partial least squares (2B-PLS) analysis to compare partition-to-partition

correlation. There are a total of six traits forming two main data partitions: topographic partition (DNE, OPCR, Slope, RFI) and performance partition (Compressive SE, and Shear SE). To assess the sensitivity of the results to subsets of the data, all of the trait comparisons were done iteratively using the total dataset, by time bin (early, middle, late Paleocene), taxon (Chinese endemic pantodonts versus non-pantodonts), and/or by dental position (all teeth, molar teeth, premolar teeth). All statistical tests were performed on 1,000 bootstrap resampled datasets that were parameterized using results of sensitivity tests on original versus cast specimen models, finite element mesh convergence tests, and time bin duration comparisons (see previous section). In addition, we quantified tooth size using two measures: total 2D surface area and square root of surface area. The R script for all statistical analyses and plots are included in Data S9.

Statistical resampling and tests

We used bootstrap resampled variance of dental topographic metrics and dental performance variables as a measure of tooth form-function disparity. 1,000 replicates of the 200-specimen DTA-FEA trait datasets were generated by sampling each DTA and FEA trait value from a uniform distribution defined using a +/-40% range of the original model-derived values. The bootstrap resampling was done with replacement, so it was possible for a given DTA/FEA trait value in a sampled tooth model to be repeated in a different replicate, but very unlikely for entire datasets to share similar values with another replicate. We used this resampling scheme to account for the uncertainty in trait estimates introduced by the totality of modeling, specimen preservation, cast versus original, and other potential sources of uncertainty in trait values. For each replicate, variance was calculated for each metric, time interval, for Chinese endemic pantodont (CEP) versus non-pantodont, and molar versus premolar data partitions. To assess shifts through time, statistical differences between the variance of each dental topographic metric sample in adjacent time intervals (A, early Paleocene; B, middle Paleocene; C, late Paleocene) were evaluated using F tests. A null hypothesis of a variance ratio of 1 between pairwise comparisons was tested using the var.test() function in R [91]. The outputs of the variance tests on a given bootstrap sample were then compiled for all 1,000 replicates, and the overall variance mean and variance test output used as the statistical basis for detecting

997 significant differences between time, taxon, and tooth data partitions. Unless indicated
998 otherwise, all tests described below were also done using the 1,000 bootstrap samples.
999 We evaluated differences in central tendency (mean value) of dental topographic
1000 metrics and dental performance variables through time using analysis of variance
1001 (ANOVA) and pairwise t tests. Each dental topographic metric was tested against the
1002 three time intervals defined above, using the aov() function in R. For statistically
1003 significant (at the $p < 0.05$ level) results, we additionally evaluated the pairwise intervals
1004 that contribute significant differences in mean dental topographic values. We assessed
1005 pairwise differences using pairwise *t* tests implemented with a Holm correction for multiple
1006 comparisons. The *t* test was conducted using pairwise.t.test() in R.
1007 We constructed a tooth morphospace using all four dental topographic metrics
1008 analyzed by principal components (PC) analysis. The first and second PC axes were
1009 chosen to visualize the two-dimensional morphospace. Additionally, we quantified the
1010 degree of morphological disparity and statistical differences in disparity between adjacent
1011 time interval data partitions. All PC scores generated from the PCA were included in the
1012 disparity analysis. The prcomp() function in R was used for PCA, and the
1013 morphol.disparity() function implemented in the Geomorph R package [92] was used for
1014 morphological disparity significance tests. Input data for the PCA were from the original
1015 dataset values, not from the bootstrap samples.
1016 Linear regression analysis between individual dental topographic metric (DNE,
1017 OPCR, Slope, RFI) and dental performance metric (compressive bite strain energy, shear
1018 bite strain energy) was performed to quantify the correlation between dental form and
1019 function. Adjusted R^2 and p values generated from the lm() function in R were used to
1020 evaluate the goodness of fit and statistical significance of the form-function relationships.
1021 The distribution of R^2 values and their corresponding p values are reported in Fig. S6.
1022 In addition to pairwise form-function linear regression analyses, we also evaluated
1023 the degree of correlation between the DTA and FEA data blocks as a means to measure
1024 covariation between dental topography and deformation resistance. We used two-block
1025 partial least squares analysis[93] coupled with bootstrap resampling to generate
1026 distributions of correlation coefficients (*r-pls*) for each of the three time bins, and then
1027 tested for significant differences in the magnitude of DTA-FEA correlation between

adjacent time bins using Welch's two-sample t tests on the correlation coefficient distributions. DTA-FEA correlation differences at $p < 0.05$ are interpreted as a significant shift in the degree of covariation of the two traits from one time bin to the next time bin.

All R scripts used in the analyses are included as supplementary files (Data S8, S9).

All data	Early-Middle Paleocene	Middle-Late Paleocene
DNE	0.7753	**0.003**
OPCR	0.0902	**0.0001**
RFI	0.605	**0.0128**
Slope	0.643	0.287
PCA Disparity	0.4562	**0.0001**
Tooth size variance	**<0.0001**	**<0.0001**
Chinese Endemic Pantodonts		
DNE	0.9264	**0.0002**
OPCR	0.17	**<0.0001**
RFI	1	1
Slope	1	1
Chinese Arctostylopids and Anagalids		
DNE	0.847	0.135
OPCR	0.47	0.18
RFI	0.2486	**0.0056**
Slope	0.642	0.269

Supplemental Document

Field locality information

The extensive development and conversion of outcrops in the Nanxiong Basin into agricultural fields has created a 'race against time' to document and study this critical area to understand placental evolution. Clyde et al. [1] estimated that 20 out of 54 early and middle Paleocene fossil sites in the Nanxiong Basin have already been destroyed by infrastructural and housing developments since their original discovery nearly three quarters of a century prior. Our re-survey of the key fossil sites during a trip there in 2023 suggests that the majority of the sites, except for the K-Pg boundary locality, which is protected by municipal historic landmark designation, are now inaccessible or completely obliterated. This reality means that the mammalian fossil samples analyzed in this study offer an ever more important and rare window into earliest mammal life during the 'Age of Mammals.' Our analyses are based on the most complete earlier Paleocene materials currently recovered from the Asian continent.

Isotope analyses show that average $\delta^{13}C$ values returned to pre K-Pg levels from a short-duration 2 ppm (part per mil) decrease about 1 Myr into the Paleocene in the Nanxiong Basin, congruent with global patterns of rapid mammal taxonomic recovery [1]. Although the majority of Paleocene fossiliferous localities are within the classic 'red beds' of south China, interbedding with limestone-like layers may indicate localized cycles of dry and humid intervals [2]. Fossil pollen in the Nanxiong Basin indicates warm climates throughout the Paleocene time interval; however, a notable shift in higher percentages of ferns and gymnosperms and lower percentage of angiosperms is observed in the late Paleocene [3], indicating local recovery of gymnosperms and ferns (Table S2).

The antipodal location of the Nanxiong Basin from the Yucatan Peninsula makes the geochemical identification of a K-Pg boundary layer difficult. Arguments for the precise location of the K-Pg boundary layer has been made on the basis of iridium enrichment in dinosaur egg shells [4] and with total mercury content that correlates with known timing of Deccan Traps volcanism [5]. Regardless of the precise stratigraphic level of the K-Pg boundary in the Nanxiong Basin, the specimens we included in our analyses have all been collected in higher stratigraphic levels that are biostratigraphically unambiguous as Paleocene sequences [3]. Planned fieldwork at and around the putative K-Pg boundary sections will sample micromammal fossils towards the objective of constructing a refined biostratigraphic framework for high-resolution analysis of the first million years of post-K-Pg mammal recovery. At this time, high-resolution data are not available to test the precise rate at which Paleocene Asian mammal taxonomic disparity and size disparity recovered/stabilized.

Evolutionary preconditions for the post-K-Pg placental radiation

Ting et al. [6] described an *in situ* faunal turnover event in southern China between the early and middle Paleocene and a gentle decrease in endemic taxa. Such a faunal change did not amount to shifting dental topographic mean values, although it is correlated with increased variability in all topographic traits (Fig. 1). Similar inferences of ecological stasis were made by Clyde et al. [7]. The replacement of some archaic taxa with more cosmopolitan ones is consistent with an evolutionary 'training ground' phenomenon where taxa preadapted to local environmental conditions were at a selective advantage to disperse into new geographic regions when global climate changed [8]. Hooker [9] makes the observation that late Paleocene North American and European mammal assemblages responded to the late Paleocene thermal maximum by increasing browsing herbivory and terrestrial taxa; this increase is at the expense of arboreal taxa in the European samples analyzed in that study. The observed DTA shifts in our dataset are consistent with this trend (Fig. 2). In the final Paleocene time bin, immediately prior to the faunal turnover that coincided with the Holarctic mammalian dispersal event and the PETM (Paleocene-Eocene Thermal Maximum), increased seasonal aridity in southern China (based on pollen composition) correlated with increased disparity and maxima of dental topographic metrics (Fig. 2).

The majority of research into post-K-Pg mammal recovery come from North American sites, which represent ~80% of known terrestrial K-Pg boundary sections [10]. By contrast, Asian K-Pg sites represent

only ~3% of K-Pg boundary sections. There are no Paleocene fossil mammal assemblages known from the Indian subcontinent [11]. Europe is similarly problematic in terms of both the paucity of well-dated K-Pg sites as well as correlated or thick stratigraphic sections that permit research into post-K-Pg dynamics [12]. Additionally, the oldest well-sampled Cenozoic mammal fauna in Europe is late early to middle Paleocene in age. This absence of earliest Paleocene data renders the study of mammalian evolutionary dynamics from the K-Pg to end-Paleocene hyperthermal event in Europe difficult [13]. Thus, no dental form-function comparisons are possible between the Asian and European post-K-Pg mammal recovery patterns for the entire Paleocene time interval.

Bayesian analyses of Paleogene mammal faunas suggest that a zoogeographic barrier between the Arabian Peninsula and the rest of Asia was present and prevented faunal interchange until the end-Oligocene [11]. Thus, the corridors of dispersal and interchange for the southern Chinese Paleocene mammals at the end-Paleocene were constrained to the north, towards the Mongolian Plateau, or to the south towards India. The absence of Paleocene Indian fossil mammals prevents a characterization of the extent to which the ecomorphological patterns described in this study also applies more broadly to fossil mammals further to the south. Based on the establishment of a land connection between Asia and India during the Paleogene, similarity in ecomorphological patterns might be expected [14]. By contrast, the well-known Paleocene-Eocene stratigraphic sequence and fossil record on the Mongolian Plateau clearly document the northward expansion of early Paleocene southern Asian taxa and the increased faunal similarity with other continents [15] during time intervals immediately following those analyzed in this study.

Absence of latitudinal gradients in Paleocene mammal taxonomic richness despite modern level temperature gradients across western interior North America suggests potential ecological instability in that region around the time of the mammalian dispersal to North America [16]. However, other analyses suggest that arrival of Eurasian immigrants to North America at the Paleocene-Eocene Thermal Maximum did not drastically alter functional diversity in the local communities [17]. Establishment of latitudinal floral gradients and the high mammal endemism in east Asia during the same time period [18] may have allowed ecological stability to establish earlier in Asia compared to North America. The stability of a large landmass in Asia for much of the Mesozoic and Cenozoic likely also contributed to the development of climate-adapted faunas in south Asia leading up to the PETM and expansion of suitable warm habitats for the southern taxa [19]. Data presented here suggest that adaptations of endemic east Asian mammals to global and regional environmental changes in the critical 10 Myr period immediately following the K-Pg extinctions can be understood as priming the evolutionary pump for the origin, radiation, and dispersal of modern mammal orders.

Summary of levels of topography-performance associations

(1) Correlation plot patterns (Fig. 3): We performed correlation plot comparisons on combined DTA and FEA data, using Kendall's τ as a measure of the strength of correlation. Contingency tables show that DNE/OPCR to compress SE/shear SE correlations increased from early to middle then late Paleocene (Fig. 3). Compared to the steady increase in integration shown by two-block PLS analyses (see below), this suggests that dental complexity and convexity were disproportionately driving the overall integration patterns, whereas cusp height and sharpness were very weakly associated to compressive and shear strain energy values.

We additionally conducted correlation analyses across time using data partitions representing individual tooth positions (Figs. S9-S11) to verify the overall trend observed using the total dataset (Fig. 3). Upper M1 patterns generally reflect the trend recovered from analysis of the overall dataset, but M2 and M3 results display inconsistent DTA-FEA correlations, possibly due to small sample sizes. Lower molar patterns generally replicate those recovered in the overall analyses, but lower M1 and M2 signals appear to be stronger than those for lower M3. Finally, low sample sizes make premolar-specific correlations unstable, with general pattern showing EP-MP strengthening then MP-LP stasis or weakening.

(2) Per-time variance patterns (Figs. S3-S5): The overall dataset showed steady increase in DNE and OPCR variance, differing from the middle Paleocene peak pattern seen in the RFI, Slope, Compressive SE, and Shear SE variances. The non-pantodont partition shows a more consistent pattern between DTA and FEA variances, with all traits showing a middle Paleocene spike. Lastly, the CEP data partition shows even more mosaic patterns than the overall data partition. CEP DNE, OPCR, and Slope show variance

increases over time, whereas Slope and compressive SE exhibit a middle Paleocene spike. Shear SE shows a steady decline in variance over time. The disaggregated molar and premolar data partitions do not contain large sample sizes; thus, we caution against over-interpreting the finer patterns until a statistical more robust sample can be analyzed. The per-tooth position analyses, although broadly supporting the early-middle Paleocene trends for both DTA and FEA data (and for FEA data in general across all time intervals), provide lower support for the middle-late Paleocene trends. Support is lowest when RFI and Slope values are analyzed by tooth position. In addition to the smaller sample sizes included in these partitioned analyses, this result may indicate that different tooth positions may record somewhat different, sometimes opposing, DTA signals but consistent FEA signals. This suggests structure-performance decoupling at the tooth position level. Similar differences between the pooled sample results and per-tooth trends when using range length (maximum trait value – minimum trait value for a given data partition) are recovered (Fig. S5B, 5D).

(3) Trait correlation patterns (Figs. S6-S7): To more precisely examine the relationships between pairs of DTA and FEA traits, we performed pairwise linear regression analyses using bootstrapped sample estimates of trait values. The outputs show that the 2B-PLS results below are mainly driven by association between higher DNE and OPCR with lower compressive and shear SE (Fig. S5). This association is particularly strong in premolar partitions and less strong in molar partitions (Fig. S6), and doesn't appear to represent differences between CEPs and non-pantodonts overall. When examined through time, there does seem to be a difference in how strongly DTA-FEA are associated; the spikes in Compressive and Shear SE values in the middle Paleocene time bin is not mirrored in DNE and OPCR values in the same time interval, suggesting a breakdown during middle Paleocene of the DTA-FEA relationship established in the early Paleocene. This result specifically mirrors findings from the CEP all-teeth data partition and non-pantodont molar partition 2B-PLS analysis (see below).

(4) Two-block partial least squares (2B-PLS) patterns (Table S1): The overall dataset exhibited a steady increase in *r* coefficient values from the early to the late Paleocene, indicating strengthening DTA-FEA integration over time. The CEP data partition showed a dip in integration in the middle Paleocene in the all-teeth partition, a steady decrease for premolar partitions, but the opposite pattern (a spike) in the molar partition. Non-pantodonts show a different pattern, where all-teeth and premolar partitions spike in integration during the middle Paleocene, whereas the molar partition dips in the middle Paleocene.

Sensitivity analyses of tooth size trends

Tooth disparity was highest during the early Paleocene time interval of our dataset; this is consistent both using variance and range length as the disparity measure (Fig. S8). The overall decrease in size disparity and variance across the Paleocene based on the total dataset was additionally tested in individual tooth position partitions (Table S3). The overall disparity trends are also observed in premolar and upper molar data partitions, whereas overall tooth size trends are observed mainly in the lower premolar 4 data partition. Decrease in mean tooth size is most consistently observed across multiple tooth partitions for the early Paleocene to late Paleocene comparison (and less clearcut for early-middle and middle-late Paleocene comparisons, respectively). Shifts during the middle Paleocene are variably supported depending on tooth position analyzed. Given that the middle Paleocene is represented by the smallest sample size, the uncertainty surrounding per-tooth position trends during this time period may be explained by the low sample available for this study.

Sample and methodological limitations

The highly fragmentary nature of early Cenozoic mammal fossils in Asia means that even the best preserved faunas studied herein contain substantial missing information. First, the absence of a high-resolution chronological framework prevents the fossil data from being analyzed on a continuous time axis; the binning of the samples into three main intervals within a 10-million-year period hinders additional hypotheses about the environmental and climatic correlations of the dental structure-performance results presented. Second, the uneven sampling of the available mammalian assemblage throughout the Paleocene sites in China limits the breadth of ecomorphological categories included in the analyses; rarer taxa representing potentially more specialized carnivore, insectivore, or herbivore forms were not included in our sampling. Third, the spatial discontinuity of stratigraphically younger (Eocene) and older (Cretaceous) mammal assemblages means that body size and ecomorphological shifts bracketing the Paleocene cannot

currently be analyzed across the sampled basins alongside the dataset presented. These limitations should be considered when interpreting the findings reported in the study.

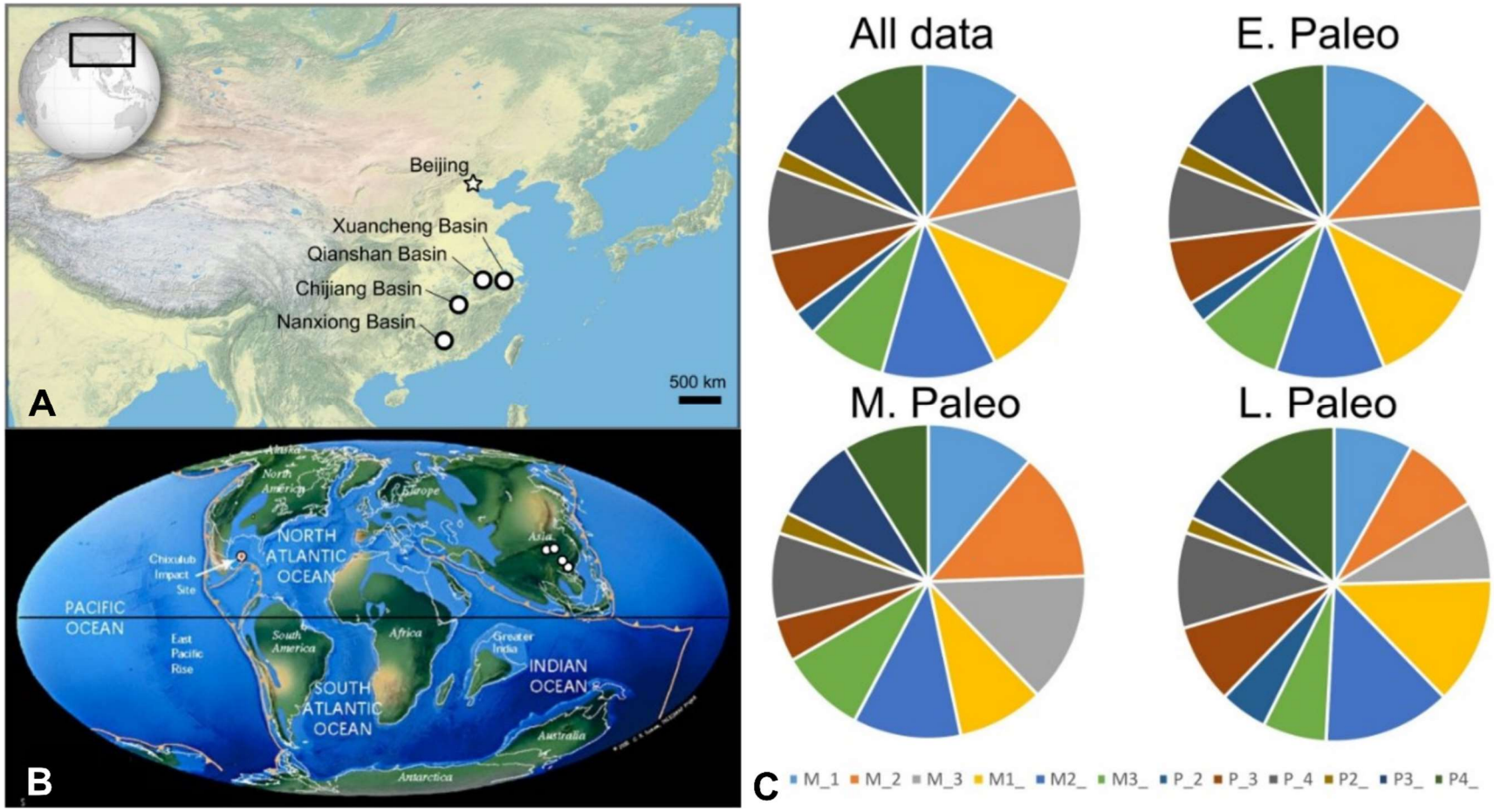

Figure S1. Maps of the fossil locality areas and proportions of teeth analyzed, related to Fig. 1. The Paleocene sedimentary basins sampled are indicated on a modern satellite image (**A**) and on a paleogeographic map of the K-Pg transition (**B**). Satellite map from NASA (www.nasa.gov) and paleogeographic map from C. Scotese (www.scotese.com)[20]. **C.** Proportions of tooth positions present in data partitions. M_1-M_3, lower first to third molars; M1_-M3_, upper first to third molars; P_2-P_4, lower second to fourth premolars; P2_-P4_, upper second to further premolars; E, early, M, middle, L, late. The middle Paleocene partition has no P_2 sampled, but otherwise the proportions of tooth positions present in each time interval are generally similar to each other.

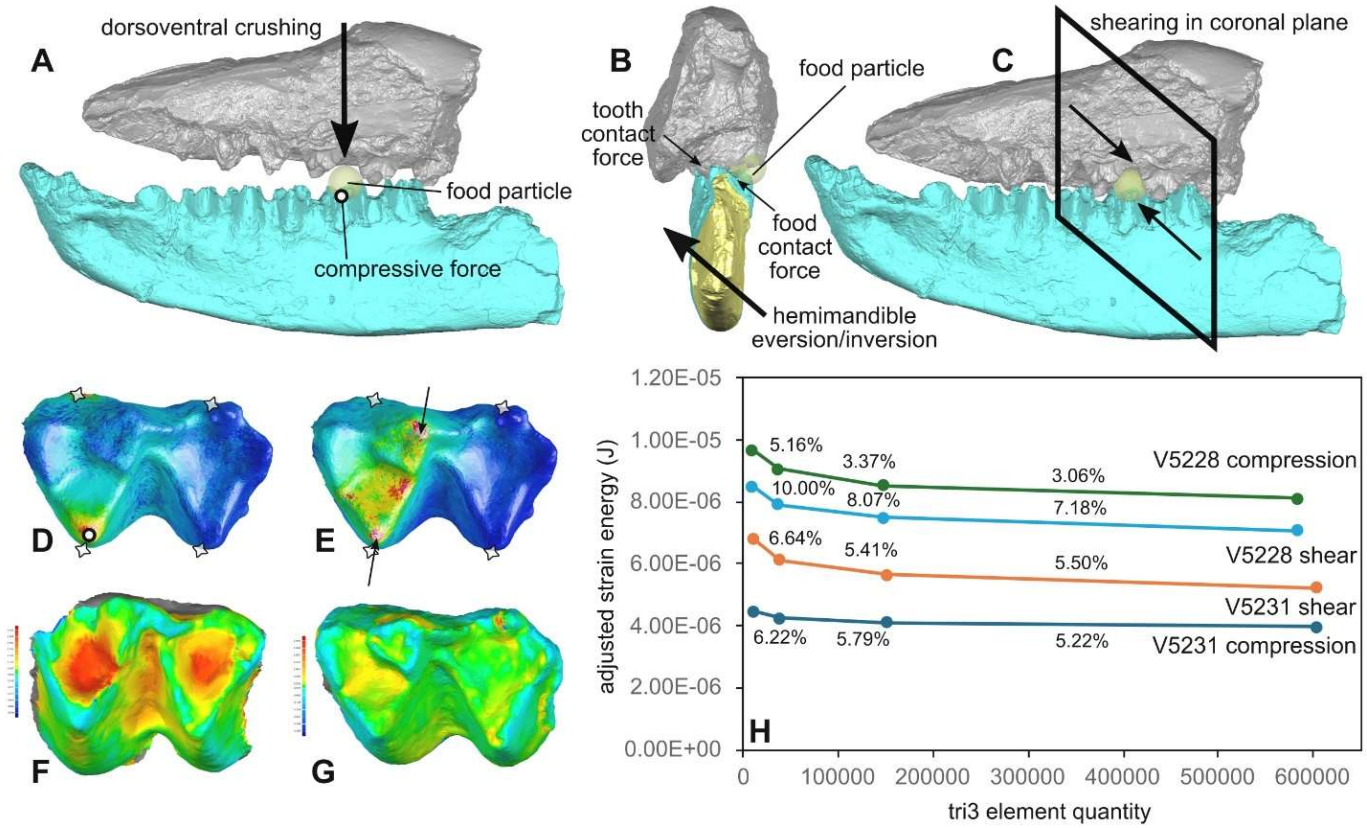

Figure S2. Finite element modeling boundary conditions and convergence tests, related to Figs. 1 and 3. (**A**) Depiction of compressive/crushing force imposed on a lower molar cusp in a specimen of *Guichilambda zhaii* (IVPP V12037) in lateral view. (**B**) Depiction of shearing motion during hemimandible eversion/inversion cycle in coronal view. (**C**) Depiction of shearing motion in lateral view. (**D**) Boundary conditions of compressive bite simulations on the lower first molar of *Altilambda tenuis* (IVPP V5231). (**E**) Boundary conditions of shearing bite simulations on *A. tenuis*. Nodal constraints are indicated by stars, compressive force by circle, and shearing forces by black arrows. (**F**) Three-dimensional deviation map of the first lower molar of *Altilambda pactus* (IVPP V5228) comparing geometric difference between models built form original versus cast-derived image data; positive (red) and negative (blue) deviation maxima +/- 0.58 mm. (**G**) Three-dimensional deviation map of the first lower molar of *Altilambda tenuis* (IVPP V5231), positive (red) and negative (blue) deviation maxima +/- 0.39 mm. (**H**) Convergence test of adjusted strain energy values (in Joules) of compression and shear bite simulations in IVPP V5228 and V5231. Percentage values indicate differences between adjacent model quantities (measured in number of three-noded triangular [tri3] elements). All model values at the lowest quantity models are considered converged based on a <=10% threshold criterion.

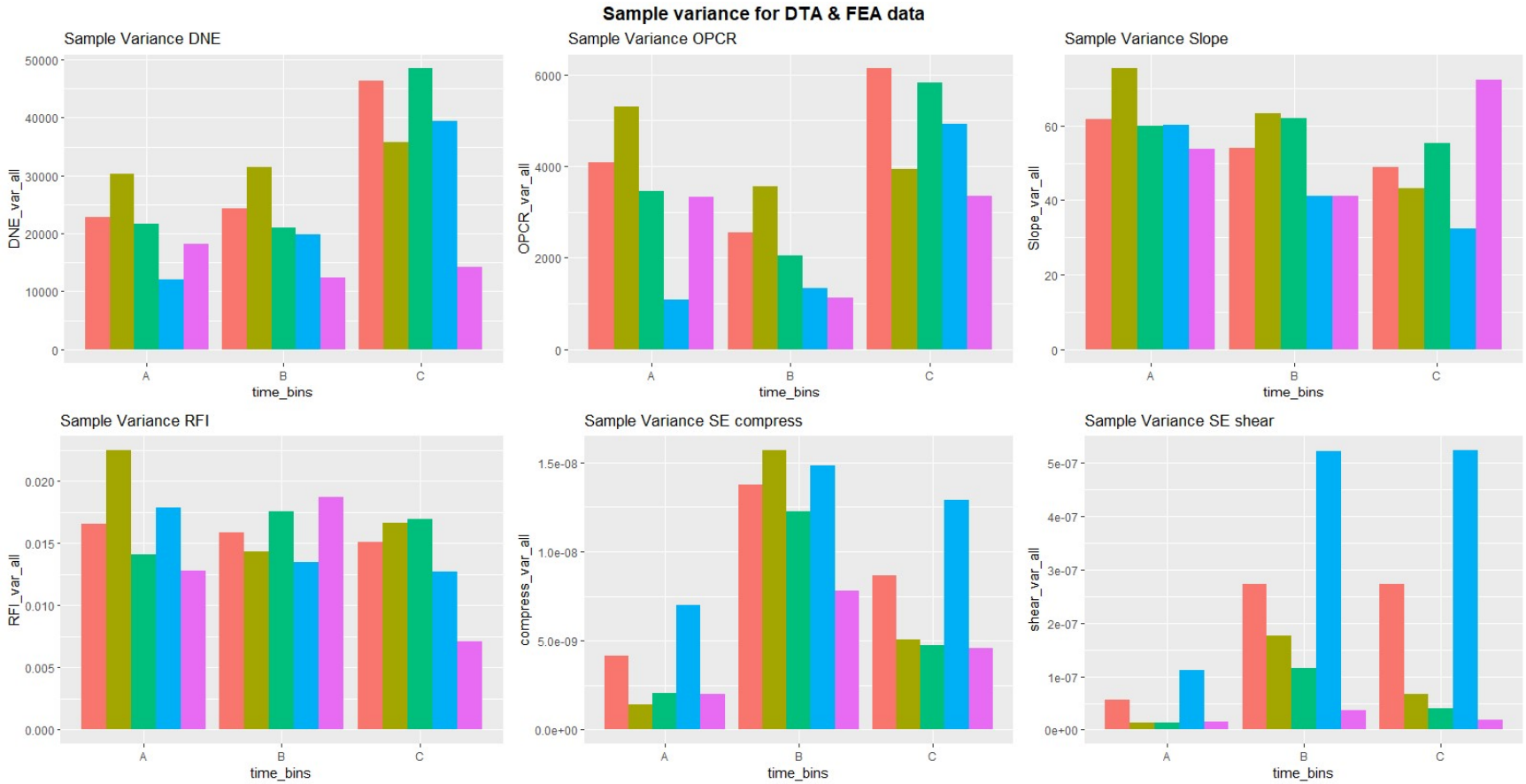

Figure S3. Sample variance (in squared units of each metric) of dental topographic metrics and dental performance traits for the overall dataset, related to Fig. 1. Time bins refer to the early Paleocene (Bin A), middle Paleocene (Bin B), and late Paleocene (Bin C). Color bars represent different data partitions: all data (salmon), all molars (teal), all premolars (green), lower molars (blue), and upper molars (purple).

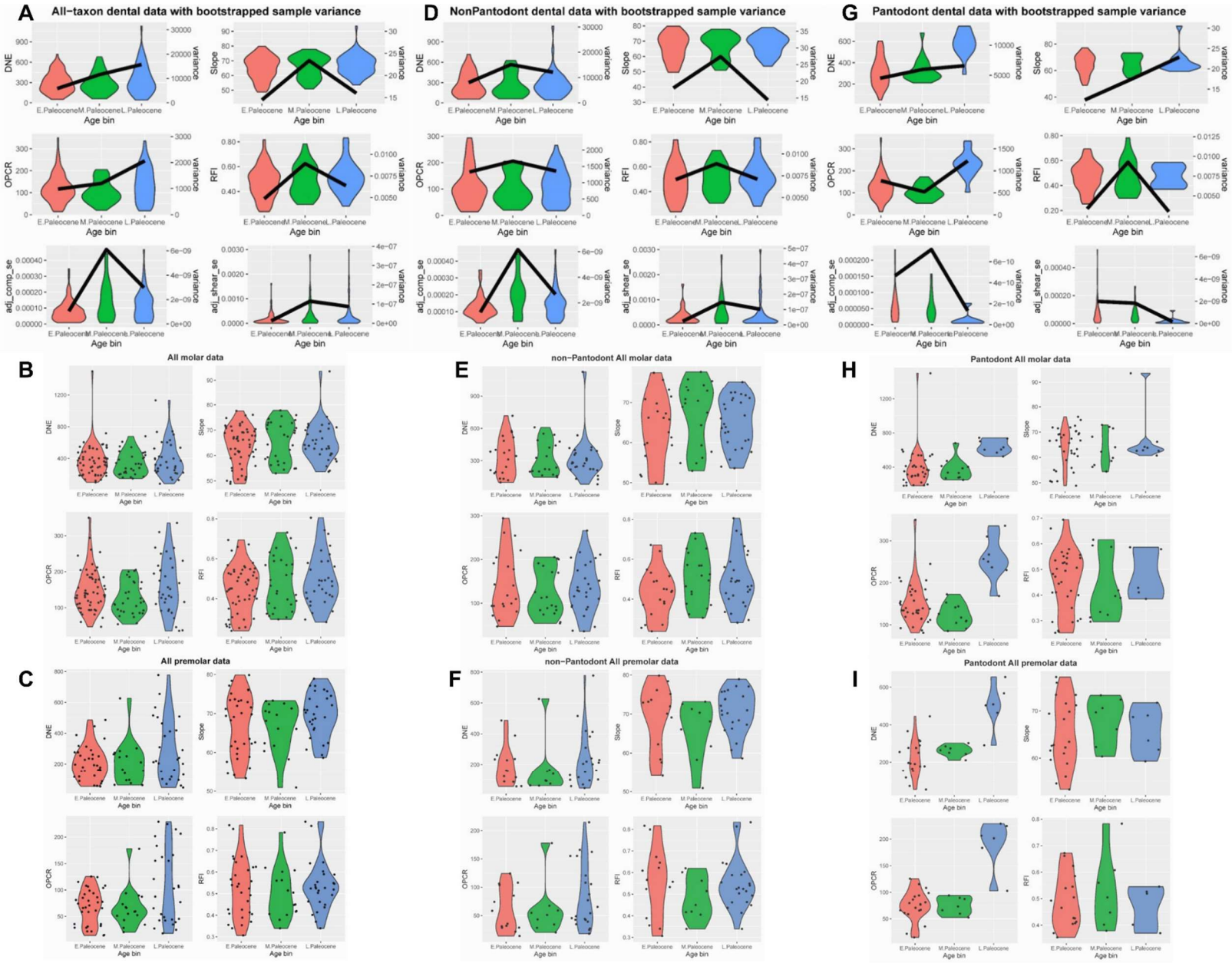
A
All-taxon dental data with bootstrapped sample variance
D
NonPantodont dental data with bootstrapped sample variance
G
Pantodont dental data with bootstrapped sample variance
B
All molar data
E
non−Pantodont All molar data
H
Pantodont All molar data
C
All premolar data
F
non−Pantodont All premolar data
I
Pantodont All premolar data
DNE
Slope
OPCR
RFI
adj_comp_se
adj_shear_se
variance
Age bin
E.Paleocene
M.Paleocene
L.Paleocene

Figure S4. Boxplots of dental topographic and finite element simulated traits, related to Table 1. Dark lines in panels A, D, and G denote sample variance per million years, calculated from 1,000 bootstrap samples of trait values pulled from uniform distributions within their estimated uncertainty ranges. The variance magnitudes are scaled to the duration of the Asian land mammal ages representing each time interval. (**A**) DTA (DNE, OPCR, Slope, RFI) and FEA (compressive bite strain energy, shear bite strain energy) boxplots representing the all tooth positions in the all-taxon partition (**B**) DTA metrics for the molar partition of all taxa. (**C**) DTA metrics for the premolar partition of all taxa. (**D**) DTA and FEA boxplots of all tooth position in the non-pantodont data partition. (**E**) DTA metrics for molars in the non-pantodont data partition. (**F**) DTA metrics for premolars in the non-pantodont data partition. (**G**) DTA and FEA boxplots of all tooth positions in the Chinese endemic pantodont (CEP) partition. (**H**) DTA metrics for molars in the CEP partition. (**I**) DTA metrics for premolars in the CEP partition.

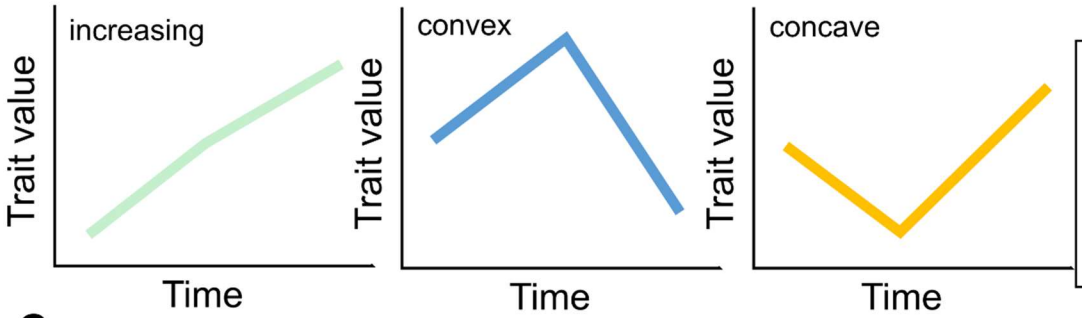

B

E-M.Paleo support	M-L.Paleo support	All trend support	
0.78/0.60	0.78/0.80	0.56/0.40	OPCR
0.89/0.90	0.78/0.80	0.67/0.70	DNE
0.44/0.50	0.56/0.50	0.22/0.40	RFI
0.67/0.70	0.44/0.30	0.44/0.30	Slope
1.00/1.00	1.00/0.80	1.00/0.80	Comp_SE
1.00/1.00	0.89/0.90	0.89/0.90	Shear_SE

C

trait	All data	lower M1	lower M2	lower M3	upper M1	upper M2	upper M3	lower P4	upper P3	upper P4
OPCR	inc	inc	inc	convex	inc	concave	concave	convex	inc	inc
DNE	inc	inc	inc	inc	inc	convex	concave	convex	inc	inc
RFI	convex	inc	convex	inc	concave	concave	concave	convex	concave	concave
Slope	convex	concave	inc	convex	concave	convex	concave	convex	inc	convex
Comp_SE	convex	convex	convex	convex	convex	convex	convex	convex	convex	convex
Shear_SE	convex	convex	convex	convex	convex	convex	convex	inc	convex	convex

D

trait	All data	lower M1	lower M2	lower M3	upper M1	upper M2	upper M3	lower P4	upper P3	upper P4
OPCR	inc	inc	inc	convex	concave	concave	concave	convex	concave	inc
DNE	inc	inc	inc	inc	inc	convex	concave	convex	inc	inc
RFI	convex	convex	convex	convex	concave	concave	concave	inc	concave	concave
Slope	inc	concave	convex	convex	concave	convex	concave	inc	inc	inc
Comp_SE	convex	convex	convex	convex	inc	convex	convex	convex	convex	inc
Shear_SE	convex	convex	convex	convex	convex	convex	convex	inc	convex	convex

Figure S5. Trends through time for DTA and FEA traits by tooth position, related to Fig. 1. (**A**) Categories of major trends observed through the three Paleocene time intervals. (**B**) Proportion of individual tooth position analyses that support the trend observed in the overall dataset. The first set of values are per-tooth variance; the second set of values are from pooled sample and per-tooth range lengths. (**C**) Individual tooth position variance trends in DTA and FEA trait values. (**D**) Individual tooth position range length trends in DTA and FEA trait values.

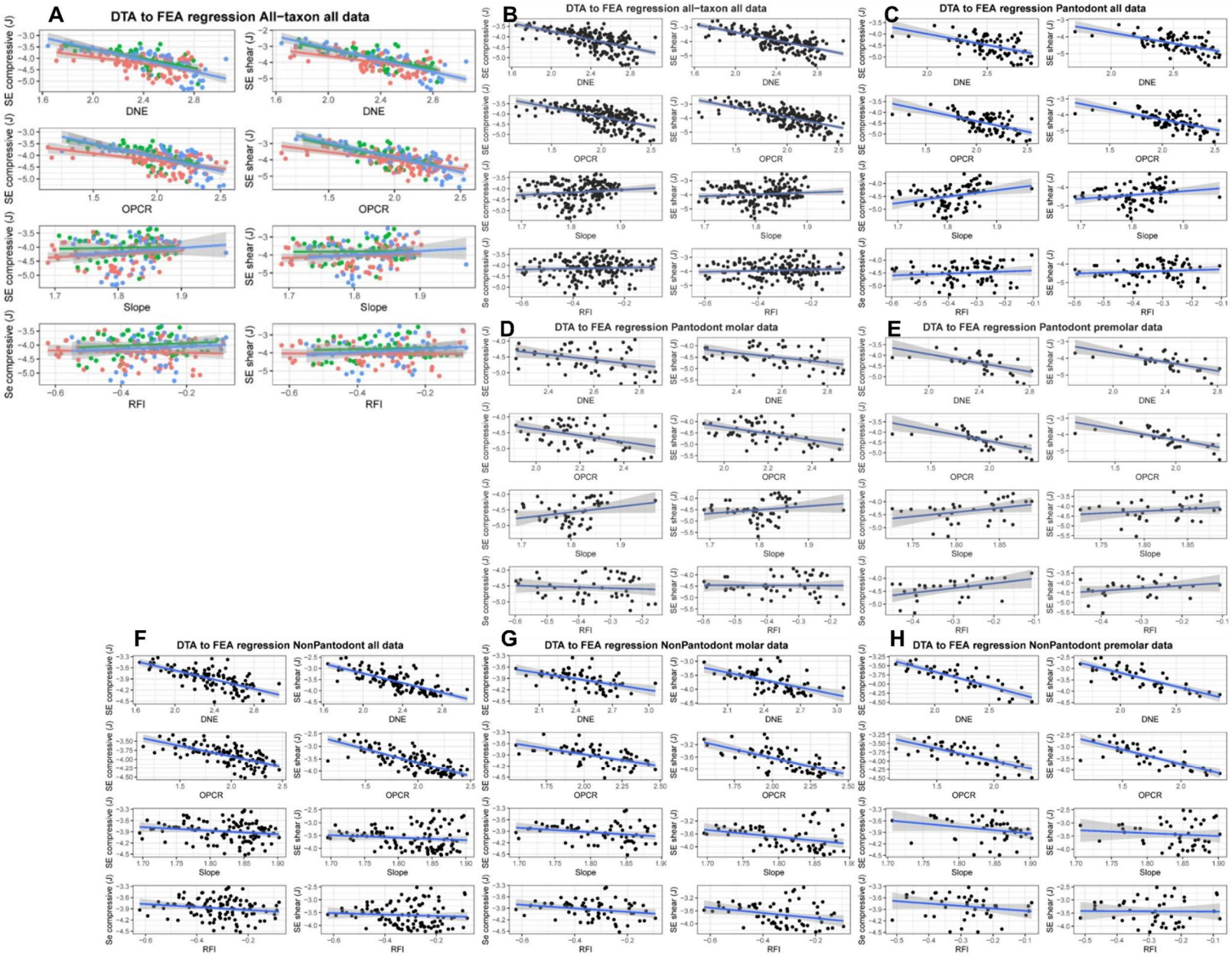
A
DTA to FEA regression All-taxon all data
B
DTA to FEA regression all-taxon all data
C
DTA to FEA regression Pantodont all data
D
DTA to FEA regression Pantodont molar data
E
DTA to FEA regression Pantodont premolar data
F
DTA to FEA regression NonPantodont all data
G
DTA to FEA regression NonPantodont molar data
H
DTA to FEA regression NonPantodont premolar data
SE compressive (J)
SE shear (J)
Se compressive (J)
DNE
OPCR
Slope
RFI

Figure S6. Linear regression analysis of dental topographic and bite performance datasets different data partitions, related to Fig. 3. (**A**) All-taxon all-teeth data partition; data points are colored according to early (red), middle (green), and late (blue) Paleocene age of the specimens. (**B**) All-taxon all-teeth data partition without time bine groups. (**C**) Chinese endemic pantodont (CEP) all-teeth data partition. (**D**) CPE molar data partition. (**E**) CEP premolar data partition. (**F**) Non-pantodont all-teeth partition. (**G**) Non-pantodont molar partition. (**H)** Non-pantodont premolar partition. Performance variables estimated using finite element analysis includes tooth crown strain energy under compressive (left column within each panel) and shear bite (right column within each panel) simulations, respectively. Rows within panels represent different DTA metrics (from top to bottom: DNE, OPCR, Slope, RFI). Fitted regression lines are shown in blue; 95% confidence envelopes are shown in gray shades.

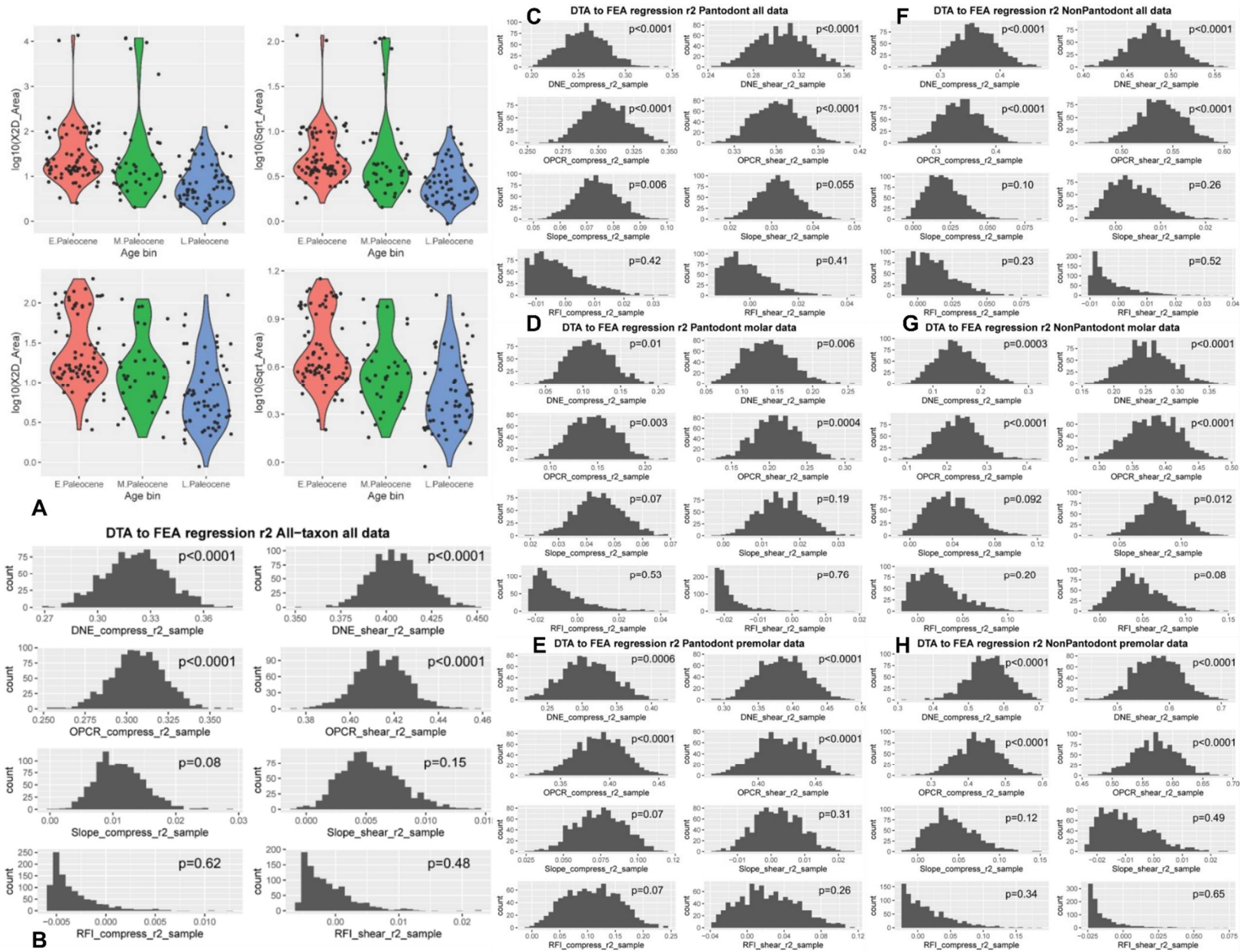
A
log10(X2D_Area)
log10(Sqrt_Area)
E.Paleocene
M.Paleocene
L.Paleocene
Age bin
B
DTA to FEA regression r2 All−taxon all data
DNE_compress_r2_sample
DNE_shear_r2_sample
OPCR_compress_r2_sample
OPCR_shear_r2_sample
Slope_compress_r2_sample
Slope_shear_r2_sample
RFI_compress_r2_sample
RFI_shear_r2_sample
p<0.0001
p=0.08
p=0.15
p=0.62
p=0.48
C
DTA to FEA regression r2 Pantodont all data
p=0.006
p=0.055
p=0.42
p=0.41
D
DTA to FEA regression r2 Pantodont molar data
p=0.01
p=0.006
p=0.003
p=0.0004
p=0.07
p=0.19
p=0.53
p=0.76
E
DTA to FEA regression r2 Pantodont premolar data
p=0.0006
p=0.07
p=0.31
p=0.07
p=0.26
F
DTA to FEA regression r2 NonPantodont all data
p=0.10
p=0.26
p=0.23
p=0.52
G
DTA to FEA regression r2 NonPantodont molar data
p=0.0003
p=0.092
p=0.012
p=0.20
p=0.08
H
DTA to FEA regression r2 NonPantodont premolar data
p=0.12
p=0.49
p=0.34
p=0.65
count

Figure S7. Tooth size boxplots and adjusted r^2 distributions from DTA-FEA linear regression analyses, related to Fig. 3. **(A)** Boxplots of tooth size by 2D area (left column within panel) or square root of 2D area (right column within panel). The top row within panel A includes sampling outliers (very large Chinese endemic pantodonts, CEPs), bottom row excludes outliers. The larger CEPs are removed in the bottom plots in order to more fully display the distribution of tooth sizes across the bimodal distribution of sizes in the main data cluster in each time bin, respectively.(B) Distribution of adjusted r^2 values from linear regression analysis of dental topographic and dental performance datasets for all-taxon all-teeth data partition. (C) CEP all-teeth partition. (D) CEP molar partition. (E) CEP premolar partition. (F) Non-pantodont all-teeth partition. (G) Non-pantodont molar partition. (H) Non-pantodont premolar partition. Adjusted r^2 values were generated from 1,000 bootstrap samples of DNE and FEA traits values for each specimen from uniform distributions that incorporate uncertainty in DNE and FEA values estimates. *P*-values calculated from *t* test of bootstrap sample *p* values against a hypothesis of $p >= 0.05$.

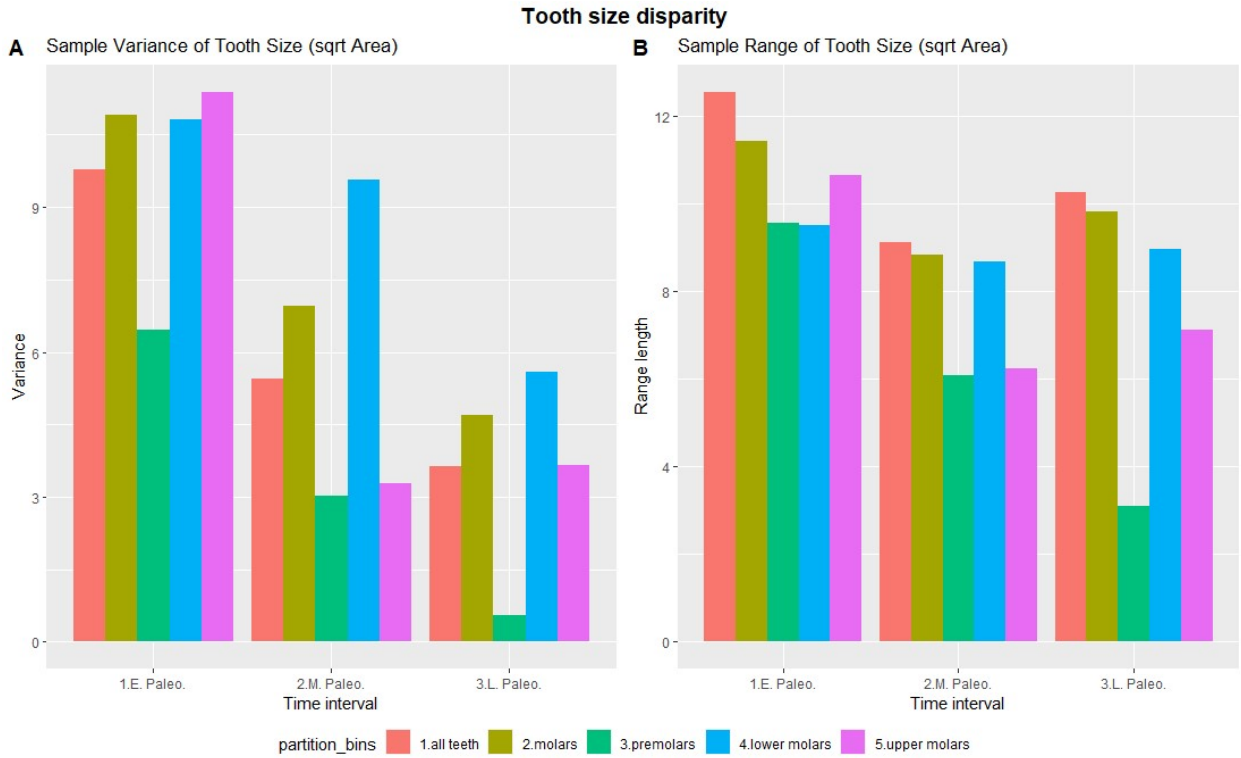

Figure S8. Tooth size disparity bar plots, related to Fig. 1. (**A**) Variance of tooth size (sqrt of 2D tooth area) in different data partitions. (**B**) Range length of tooth size (sqrt of 2D tooth area) in different partitions.

all data EP to MP

DNE	0.58	0.22	0.15	-0.29	-0.36
0.67	OPCR	0.02	0	-0.29	-0.37
0.29	0.09	Slope	0.52	0.12	0.09
0.22	0.1	0.69	RFI	-0.07	-0.04
-0.41	-0.34	0.02	0.05	Compress	0.66
-0.4	-0.37	0.07	0.03	0.75	Shear

all data MP to LP

DNE	0.67	0.29	0.22	-0.41	-0.4
0.71	OPCR	0.09	0.1	-0.34	-0.37
-0.07	-0.18	Slope	0.69	0.02	0.07
0.02	-0.12	0.36	RFI	0.05	0.03
-0.56	-0.5	0.1	0.05	Compress	0.75
-0.61	-0.56	0.08	0.04	0.68	Shear

upper M1 data EP to MP

DNE	0.47	0.29	0.16	-0.38	-0.29
1	OPCR	0.2	-0.02	-0.11	-0.11
0.33	0.33	Slope	0.69	-0.2	-0.11
-0.33	-0.33	0.33	RFI	-0.33	-0.16
-0.33	-0.33	-1	-0.33	Compress	0.73
-0.33	-0.33	-1	-0.33	1	Shear

upper M1 data MP to LP

DNE	1	0.33	-0.33	-0.33	-0.33
0.47	OPCR	0.33	-0.33	-0.33	-0.33
0.07	0.6	Slope	0.33	-1	-1
0.07	-0.2	0.2	RFI	-0.33	-0.33
-0.6	-0.87	-0.47	0.07	Compress	1
-0.47	-0.73	-0.33	0.2	0.87	Shear

upper M2 data EP to MP

DNE	0.5	0.56	0.56	-0.78	-0.65
0.33	OPCR	0.17	0.5	-0.61	-0.82
0.67	0.67	Slope	0.33	-0.44	-0.37
-0.33	-0.33	0	RFI	-0.67	-0.54
-1	-0.33	-0.67	0.33	Compress	0.76
-1	-0.33	-0.67	0.33	1	Shear

upper M2 data MP to LP

DNE	0.33	0.67	-0.33	-1	-1
0.43	OPCR	0.67	-0.33	-0.33	-0.33
0.24	0.24	Slope	0	-0.67	-0.67
-0.05	0.14	0.33	RFI	0.33	0.33
-0.43	-0.24	-0.81	-0.33	Compress	1
-0.62	-0.81	-0.24	0.05	0.43	Shear

upper M3 data EP to MP

DNE	0.71	0.36	0.43	-0.57	-0.43
0.33	OPCR	0.64	0.57	-0.71	-0.57
1	0.33	Slope	0.93	-0.5	-0.36
-0.33	-1	-0.33	RFI	-0.43	-0.29
-0.67	-0.67	-0.67	0.67	Compress	0.71
-1	-0.33	-1	0.33	0.67	Shear

upper M3 data MP to LP

DNE	0.33	1	-0.33	-0.67	-1
0.33	OPCR	0.33	-1	-0.67	-0.33
0.33	0.33	Slope	-0.33	-0.67	-1
0	0.67	0	RFI	0.67	0.33
0	0	0.67	-0.33	Compress	0.67
-0.67	-0.67	0	-0.33	0.33	Shear

Figure S9. Correlation through time plots for upper molar DTA and FEA data, related to Fig. 3. The upper diagonal in the left column shows early Paleocene (EP) correlations, the lower diagonal in the left column shows middle Paleocene (MP) correlations. The upper diagonal in the right column shows middle Paleocene correlations, and the lower diagonal in the right column shows late Paleocene (LP) correlations. Red boxes indicate correlations between DTA and FEA traits. Dark gray boxes indicate decoupling of correlation directions across time intervals. Upper M1 patterns general reflect the trend recovered from analysis of the overall dataset, but M2 and M3 results display inconsistent DTA-FEA correlations, possibly due to small sample sizes.

all data EP to MP

DNE	0.58	0.22	0.15	-0.29	-0.36
0.67	OPCR	0.02	0	-0.29	-0.37
0.29	0.09	Slope	0.52	0.12	0.09
0.22	0.1	0.69	RFI	-0.07	-0.04
-0.41	-0.34	0.02	0.05	Compress	0.66
-0.4	-0.37	0.07	0.03	0.75	Shear

all data MP to LP

DNE	0.67	0.29	0.22	-0.41	-0.4
0.71	OPCR	0.09	0.1	-0.34	-0.37
-0.07	-0.18	Slope	0.69	0.02	0.07
0.02	-0.12	0.36	RFI	0.05	0.03
-0.56	-0.5	0.1	0.05	Compress	0.75
-0.61	-0.56	0.08	0.04	0.68	Shear

lower M1 data EP to MP

DNE	0.72	0.22	0.39	-0.17	-0.33
0.4	OPCR	-0.06	0.22	-0.44	-0.28
0.6	0	Slope	0.28	0.28	0
0	-0.2	0.4	RFI	0.11	-0.28
-0.4	-0.6	0	0.2	Compress	0.61
-0.2	-0.8	0.2	0.4	0.8	Shear

lower M1 data MP to LP

DNE	0.4	0.6	0	-0.4	-0.2
0.6	OPCR	0	-0.2	-0.6	-0.8
0	-0.4	Slope	0.4	0	0.2
0	-0.4	0.6	RFI	0.2	0.4
-0.6	-0.6	0.4	0	Compress	0.8
-0.2	-0.6	0.4	0	0.6	Shear

lower M2 data EP to MP

DNE	0.47	-0.07	0.29	0.16	-0.07
0.73	OPCR	-0.42	0.02	0.24	-0.16
0.73	0.73	Slope	0.11	0.16	-0.07
0.2	0.2	0.47	RFI	-0.38	-0.16
-0.2	-0.47	-0.2	0.07	Compress	0.16
-0.87	-0.6	-0.6	-0.33	0.33	Shear

lower M2 data MP to LP

DNE	0.73	0.73	0.2	-0.2	-0.87
0.6	OPCR	0.73	0.2	-0.47	-0.6
-0.2	-0.6	Slope	0.47	-0.2	-0.6
0	-0.4	0.4	RFI	0.07	-0.33
-0.6	-0.6	0.2	0	Compress	0.33
-0.6	-0.6	0.2	0	1	Shear

lower M3 data EP to MP

DNE	-0.05	0.05	-0.24	-0.05	-0.33
0.33	OPCR	0.14	0.05	0.24	0.33
0.33	-0.07	Slope	0.33	0.14	0.43
0.87	0.47	0.2	RFI	-0.14	0.33
-0.2	-0.6	0.47	-0.33	Compress	0.52
-0.33	-0.73	0.07	-0.47	0.6	Shear

lower M3 data MP to LP

DNE	0.33	0.33	0.87	-0.2	-0.33
0.8	OPCR	-0.07	0.47	-0.6	-0.73
0.4	0.2	Slope	0.2	0.47	0.07
0.2	0	0.4	RFI	-0.33	-0.47
-0.6	-0.4	-0.4	-0.6	Compress	0.6
-0.2	0	0	-0.2	0.6	Shear

Figure S10. Correlation through time plots for lower molar DTA and FEA data, related to Fig. 3. The upper diagonal in the left column shows early Paleocene (EP) correlations, the lower diagonal in the left column shows middle Paleocene (MP) correlations. The upper diagonal in the right column shows middle Paleocene correlations, and the lower diagonal in the right column shows late Paleocene (LP) correlations. Red boxes indicate correlations between DTA and FEA traits. Dark gray boxes indicate decoupling of correlation directions across time intervals. Lower molar patterns generally replicate those recovered in the overall analyses, but lower M1 and M2 signals appear to be stronger than those for lower M3.

all data EP to MP

DNE	0.58	0.22	0.15	-0.29	-0.36
0.67	OPCR	0.02	0	-0.29	-0.37
0.29	0.09	Slope	0.52	0.12	0.09
0.22	0.1	0.69	RFI	-0.07	-0.04
-0.41	-0.34	0.02	0.05	Compress	0.66
-0.4	-0.37	0.07	0.03	0.75	Shear

all data MP to LP

DNE	0.67	0.29	0.22	-0.41	-0.4
0.71	OPCR	0.09	0.1	-0.34	-0.37
-0.07	-0.18	Slope	0.69	0.02	0.07
0.02	-0.12	0.36	RFI	0.05	0.03
-0.56	-0.5	0.1	0.05	Compress	0.75
-0.61	-0.56	0.08	0.04	0.68	Shear

lower P4 data EP to MP

DNE	0.2	0.6	-0.07	-0.47	-0.33
1	OPCR	0.07	-0.33	-0.2	-0.6
0.33	0.33	Slope	-0.2	-0.33	-0.2
0	0	0.67	RFI	-0.47	0.2
-1	-1	-0.33	0	Compress	0.07
-0.67	-0.67	-0.67	-0.33	0.67	Shear

lower P4 data MP to LP

DNE	1	0.33	0	-1	-0.67
0.6	OPCR	0.33	0	-1	-0.67
-0.07	-0.47	Slope	0.67	-0.33	-0.67
-0.33	-0.73	0.47	RFI	0	-0.33
-0.73	-0.6	0.07	0.33	Compress	0.67
-0.87	-0.73	0.2	0.47	0.87	Shear

upper P3 data EP to MP

DNE	0.14	0.43	0.71	-0.93	-0.57
0.67	OPCR	0.29	-0.14	-0.07	-0.43
0.67	0.33	Slope	0.43	-0.5	-0.43
0	0.33	0.33	RFI	-0.79	-0.43
-1	-0.67	-0.67	0	Compress	0.64
-0.67	-0.33	-1	-0.33	0.67	Shear

upper P3 data MP to LP

DNE	0.67	0.67	0	-1	-0.67
-0.33	OPCR	0.33	0.33	-0.67	-0.33
-0.33	-0.33	Slope	0.33	-0.67	-1
-1	0.33	0.33	RFI	0	-0.33
-0.33	-0.33	1	0.33	Compress	0.67
0.33	-1	0.33	-0.33	0.33	Shear

upper P4 data EP to MP

DNE	0.47	0.47	0.2	-0.87	-0.6
1	OPCR	0.2	-0.33	-0.33	-0.33
0.33	0.33	Slope	0.47	-0.33	-0.07
0.33	0.33	0.33	RFI	-0.07	0.2
-1	-1	-0.33	-0.33	Compress	0.73
-0.67	-0.67	-0.67	-0.67	0.67	Shear

upper P4 data MP to LP

DNE	1	0.33	0.33	-1	-0.67
0.71	OPCR	0.33	0.33	-1	-0.67
0.43	0.14	Slope	0.33	-0.33	-0.67
0.43	0.14	0.43	RFI	-0.33	-0.67
-0.43	-0.71	-0.05	0.14	Compress	0.67
-0.43	-0.71	-0.05	0.14	0.81	Shear

Figure S11. Correlation through time plots for premolar DTA and FEA data, related to Fig. 3. The upper diagonal in the left column shows early Paleocene (EP) correlations, the lower diagonal in the left column shows middle Paleocene (MP) correlations. The upper diagonal in the right column shows middle Paleocene correlations, and the lower diagonal in the right column shows late Paleocene (LP) correlations. Red boxes indicate correlations between DTA and FEA traits. Dark gray boxes indicate decoupling of correlation directions across time intervals. Low sample sizes make premolar correlations unstable, with general pattern showing EP-MP strengthening then MP-LP stasis or weakening

Taxon	Dentition	early Paleocene	middle Paleocene	late Paleocene
1. All Taxa	All	0.40	0.48	0.52
2. Chinese endemic pantodonts	All	0.30	0.29	0.43
	Premolar	0.69	0.57	0.51
	Molar	0.15	0.70	0.65
3. Non-pantodont mammals	All	0.48	0.53	0.49
	Premolar	0.50	0.52	0.55
	Molar	0.45	0.40	0.46

Table S1. Two-block partial least squares (PLS) *r* coefficients from bootstrapped analyses, related to Fig. 3. 1,000 bootstrap samples of DTA and FEA values were taken from uniform distributions of trait uncertainty ranges, and two-block partial east squared analysis conducted on each sample for early-middle Paleocene and middle-late Paleocene data partition pairings, respectively. All *r* values are statistically significantly different ($p < 0.05$) between adjacent time intervals, based on a one-sample t test of the distribution of 1,000 p values from the bootstrap two-block PLS samples against $p < 0.05$.

	E. Paleocene	M. Paleocene	L. Paleocene
Angiosperms	75-88%	84%	50-65%
Ferns	11-20%	11%	25-33%
Gymnosperms	1-5%	5%	10-18%

Table S2. Relative percentages of fossil pollen found in the Nanxiong Basin, Related to Fig. 2 and based on [3].

Measure	Trait	Statistic	All	m/1	m/2	m/3	M1/	M2/	M3/	p/4	P3/	P4/
Sample Size	Early Paleocene (EP)		79	10	11	8	10	10	8	7	8	7
	Middle Paleocene (MP)		42	5	6	6	4	5	4	4	4	4
	Late Paleocene (LP)		52	5	5	5	8	8	4	6	3	8
Mean Disparity	Area	var.test EP-MP	0.00	0.44	0.81	0.78	0.02	0.97	0.01	0.00	0.54	0.04
		var.test MP-LP	0.03	0.00	0.06	0.92	0.14	0.00	0.04	0.08	0.05	0.24
	Sqrt Area	var.test EP-MP	0.06	0.59	0.56	0.59	0.13	0.74	0.14	0.04	0.44	0.12
		var.test MP-LP	0.16	0.02	0.11	0.72	0.28	0.06	0.07	0.30	0.17	0.72
Mean Size	Area	t.test EP-MP	0.00	0.18	1.00	1.00	0.75	0.91	0.06	0.04	0.86	0.53
		t.test MP-LP	0.01	0.18	1.00	1.00	0.75	0.18	0.40	0.04	0.34	0.03
		t.test EP-LP	0.00	0.01	1.00	1.00	0.75	0.02	0.01	0.00	0.34	0.00
	Sqrt Area	t.test EP-MP	0.00	0.18	1.00	1.00	0.75	0.91	0.06	0.04	0.86	0.53
		t.test MP-LP	0.01	0.18	1.00	1.00	0.75	0.18	0.40	0.04	0.34	0.03
		t.test EP-LP	0.00	0.01	1.00	1.00	0.75	0.02	0.01	0.00	0.34	0.00

Table S3. Sample size, disparity, and mean tooth size by tooth position. Related to Fig. 1. Mean disparity difference is measured by pair-wise variance tests (var.test); mean tooth size difference is measured by pairwise *t* tests (t.test). *p* values <=0.05 are shaded. Overall disparity trends are also observed in premolar and upper molar data partitions, whereas overall tooth size trends are observed mainly in the lower premolar 4 data partition. Decrease in mean tooth size is most consistently observe across multiple tooth partitions for the early Paleocene to late Paleocene comparison.

Supplemental references

[1] W. C. Clyde *et al.*, “New paleomagnetic and stable-isotope results from the Nanxiong Basin, China: implications for the K/T boundary and the timing of Paleocene mammalian turnover,” *J. Geol.*, vol. 118, no. 2, pp. 131–143, 2010.

[2] Z. Xie, X. Liu, X. Mao, Z. Le, and C. Peng, “Paleoenvironment of Eocene Red Beds in the Nanxiong Basin,” *Trop. Geogr.*, vol. 39, no. 2, pp. 218–228, 2019.

[3] X.-Q. Zhang, S.-J. Zhang, X.-Y. Lin, Q.-J. Huang, and H.-L. Li, *The red beds and paleontology of Nanxiong Basin*. Beijing: Huaxia Publishing House, 2021.

[4] Z. Zhao *et al.*, “A possible causal relationship between extinction of dinosaurs and K/T iridium enrichment in the Nanxiong Basin, South China: evidence from dinosaur eggshells,” *Palaeogeogr. Palaeoclimatol. Palaeoecol.*, vol. 178, no. 1, pp. 1–17, 2002, doi: https://doi.org/10.1016/S0031-0182(01)00361-3.

[5] M. Zhao, M. Ma, M. He, Y. Qiu, and X. Liu, “Evaluation of the four potential Cretaceous-Paleogene (K-Pg) boundaries in the Nanxiong Basin based on evidences from volcanic activity and paleoclimatic evolution,” *Sci. China Earth Sci.*, vol. 64, no. 4, pp. 631–641, 2021, doi: 10.1007/s11430-020-9736-0.

[6] S.-Y. Ting, Y.-S. Tong, W. C. Clyde, and P. L. Koch, “Asian early Paleogene chronology and mammalian faunal turnover events,” *Vertebr. Palasiat.*, vol. 49, no. 1, pp. 1–28, 2011.

[7] W. C. Clyde *et al.*, “An integrated stratigraphic record from the Paleocene of the Chijiang Basin, Jiangxi Province (China): Implications for mammalian turnover and Asian block rotations,” *Earth Planet. Sci. Lett.*, vol. 269, no. 3–4, pp. 554–564, 2008.

[8] T. Deng *et al.*, “Out of Tibet: Pliocene Woolly Rhino Suggests High-Plateau Origin of Ice Age Megaherbivores,” *Science (80-.).*, vol. 333, no. 6047, pp. 1285 LP – 1288, Sep. 2011, doi: 10.1126/science.1206594.

[9] J. J. Hooker, “Paleogene mammals: crises and ecological change,” *Biot. response to Glob. Chang. last*, vol. 145, pp. 333–349, 2000.

[10] V. Vajda and A. Bercovici, “The global vegetation pattern across the Cretaceous–Paleogene mass extinction interval: a template for other extinction events,” *Glob. Planet. Change*, vol. 122, pp. 29–49, 2014.

[11] X. Ni *et al.*, “Paleogene mammalian fauna exchanges and the paleogeographic pattern in Asia,” *Sci. China Earth Sci.*, vol. 63, pp. 202–211, 2020.

[12] Z. Csiki-Sava, E. Buffetaut, A. Ősi, X. Pereda-Suberbiola, and S. L. Brusatte, “Island life in the Cretaceous-faunal composition, biogeography, evolution, and extinction of land-living vertebrates on the Late Cretaceous European archipelago,” *Zookeys*, no. 469, pp. 1–161, 2015.

[13] E. De Bast and T. Smith, “The oldest Cenozoic mammal fauna of Europe: implication of the Hainin reference fauna for mammalian evolution and dispersals during the Paleocene,” *J. Syst. Palaeontol.*, vol. 15, no. 9, pp. 741–785, 2017.

[14] X. Hu, E. Garzanti, T. Moore, and I. Raffi, “Direct stratigraphic dating of India-Asia collision onset at the Selandian (middle Paleocene, 59±1 Ma),” *Geology*, vol. 43, no. 10, pp. 859–862, 2015.

[15] Y. Wang *et al.*, “Early Paleogene stratigraphic sequences, mammalian evolution and its response to environmental changes in Erlian Basin, Inner Mongolia, China,” *Sci. China Earth Sci.*, vol. 53, pp. 1918–1926, 2010.

[16] P. J. Rose, D. L. Fox, J. Marcot, and C. Badgley, “Flat latitudinal gradient in Paleocene mammal richness suggests decoupling of climate and biodiversity,” *Geology*, vol. 39, no. 2, pp. 163–166, 2011.

[17] D. Fraser and S. K. Lyons, “Mammal community structure through the Paleocene-Eocene thermal maximum,” *Am. Nat.*, vol. 196, no. 3, pp. 271–290, 2020.

[18] Z. Qiu and C. Li, “Evolution of Chinese mammalian faunal regions and elevation of the Qinghai-Xizang (Tibet) Plateau,” *Sci. China Ser. D Earth Sci.*, vol. 48, pp. 1246–1258, 2005.

[19] K. C. Beard, “East of Eden: Asia as an important center of taxonomic origination in mammalian evolution,” *Bull. Carnegie Museum Nat. Hist.*, vol. 34, pp. 5–39, 1998.

[20] C. R. Scotese, *Atlas of Earth History, Volume 1, Paleogeography*. Arlington, Texas: PALEOMAP Project, 2001.

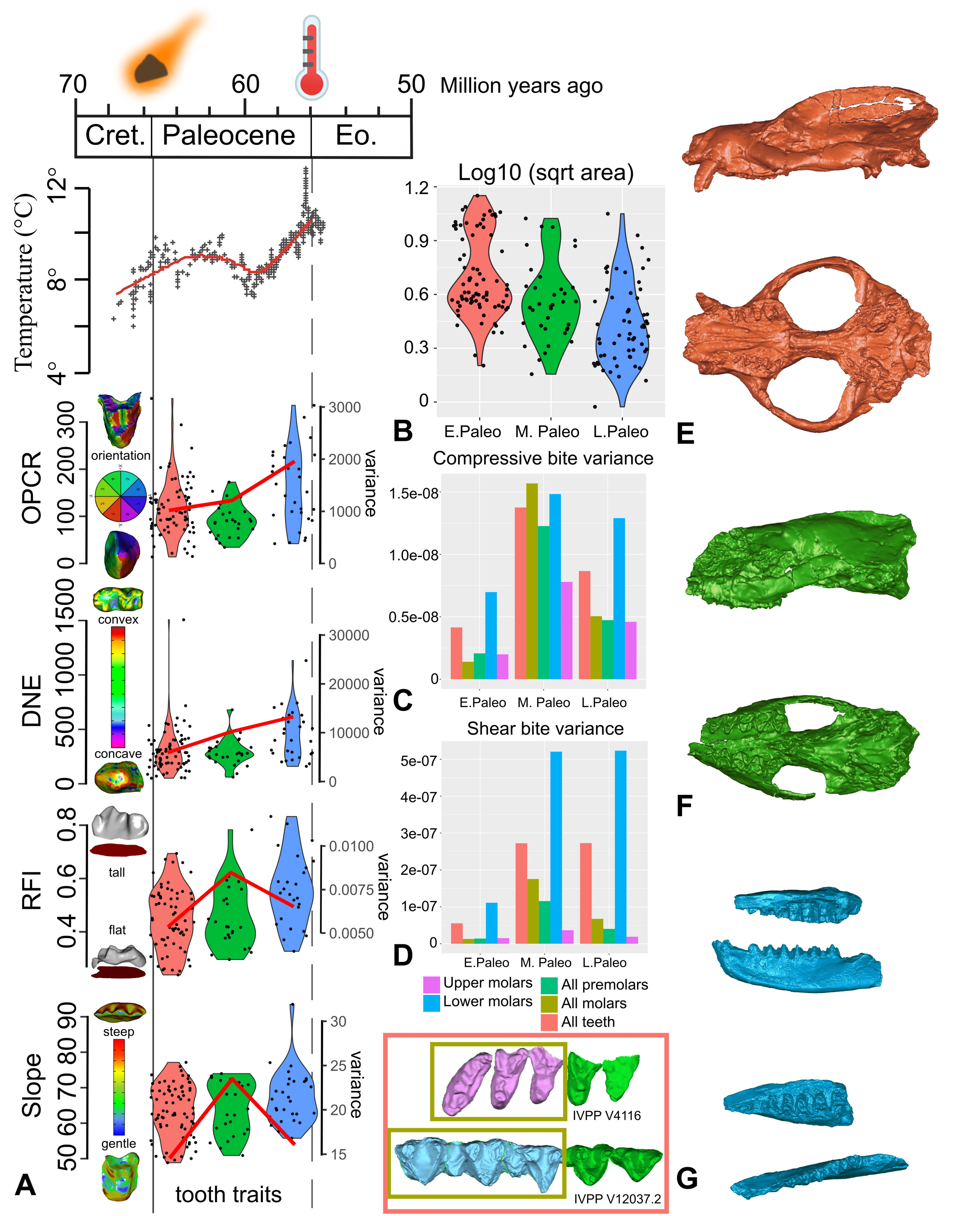
70
60
50
Million years ago
Cret.
Paleocene
Eo.
Temperature (°C)
12°
8°
4°
OPCR
orientation
convex
DNE
concave
RFI
tall
flat
Slope
steep
gentle
variance
tooth traits
A
Log10 (sqrt area)
B
Compressive bite variance
C
Shear bite variance
D
E.Paleo
M. Paleo
L.Paleo
Upper molars
Lower molars
All premolars
All molars
All teeth
IVPP V4116
IVPP V12037.2
E
F
G

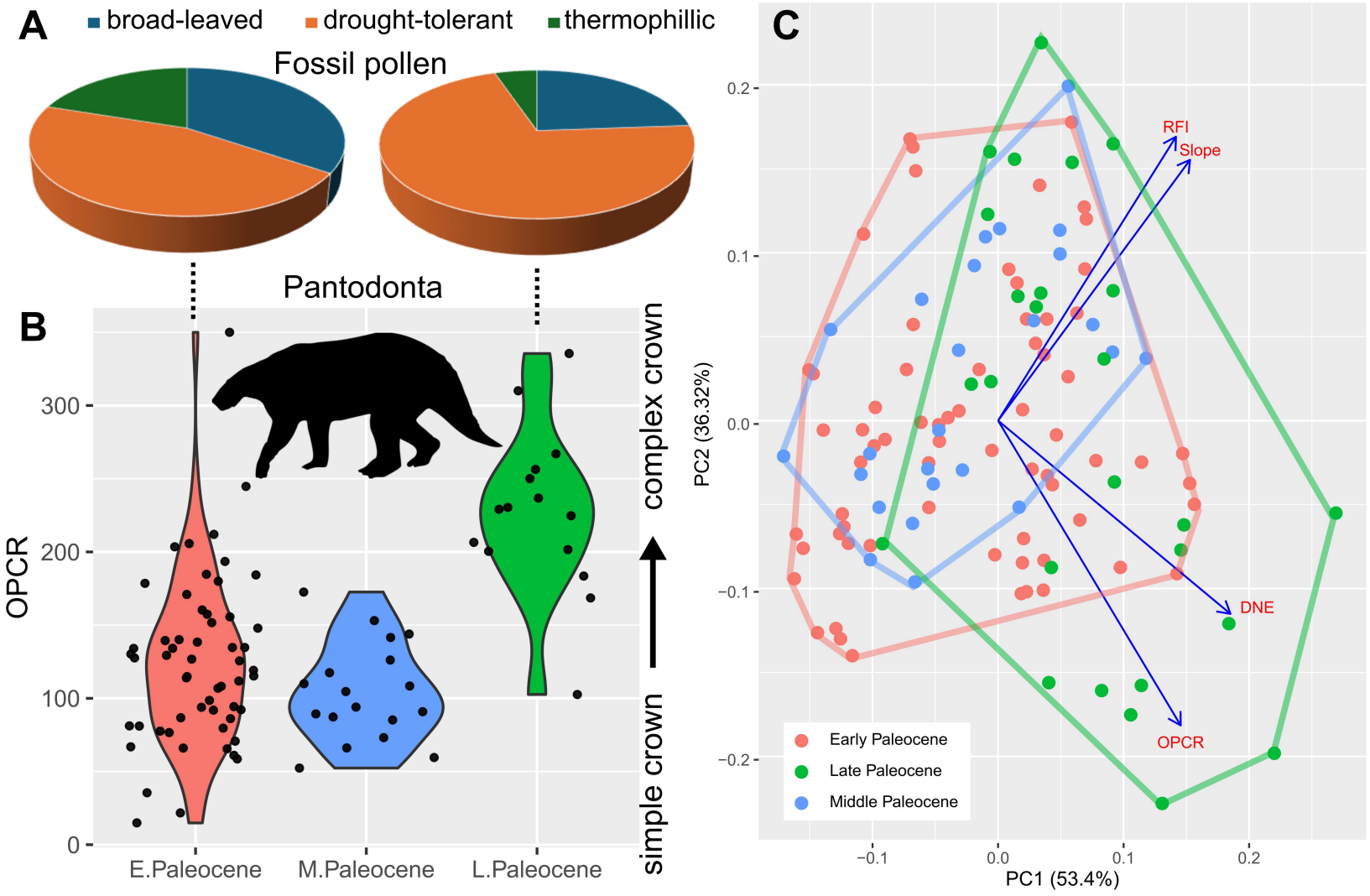
A
broad-leaved
drought-tolerant
thermophillic
Fossil pollen
Pantodonta
B
OPCR
300
200
100
0
E.Paleocene
M.Paleocene
L.Paleocene
complex crown
simple crown
C
RFI
Slope
DNE
OPCR
Early Paleocene
Late Paleocene
Middle Paleocene
PC2 (36.32%)
PC1 (53.4%)
0.2
0.1
0.0
−0.1
−0.2
−0.1
0.0
0.1
0.2

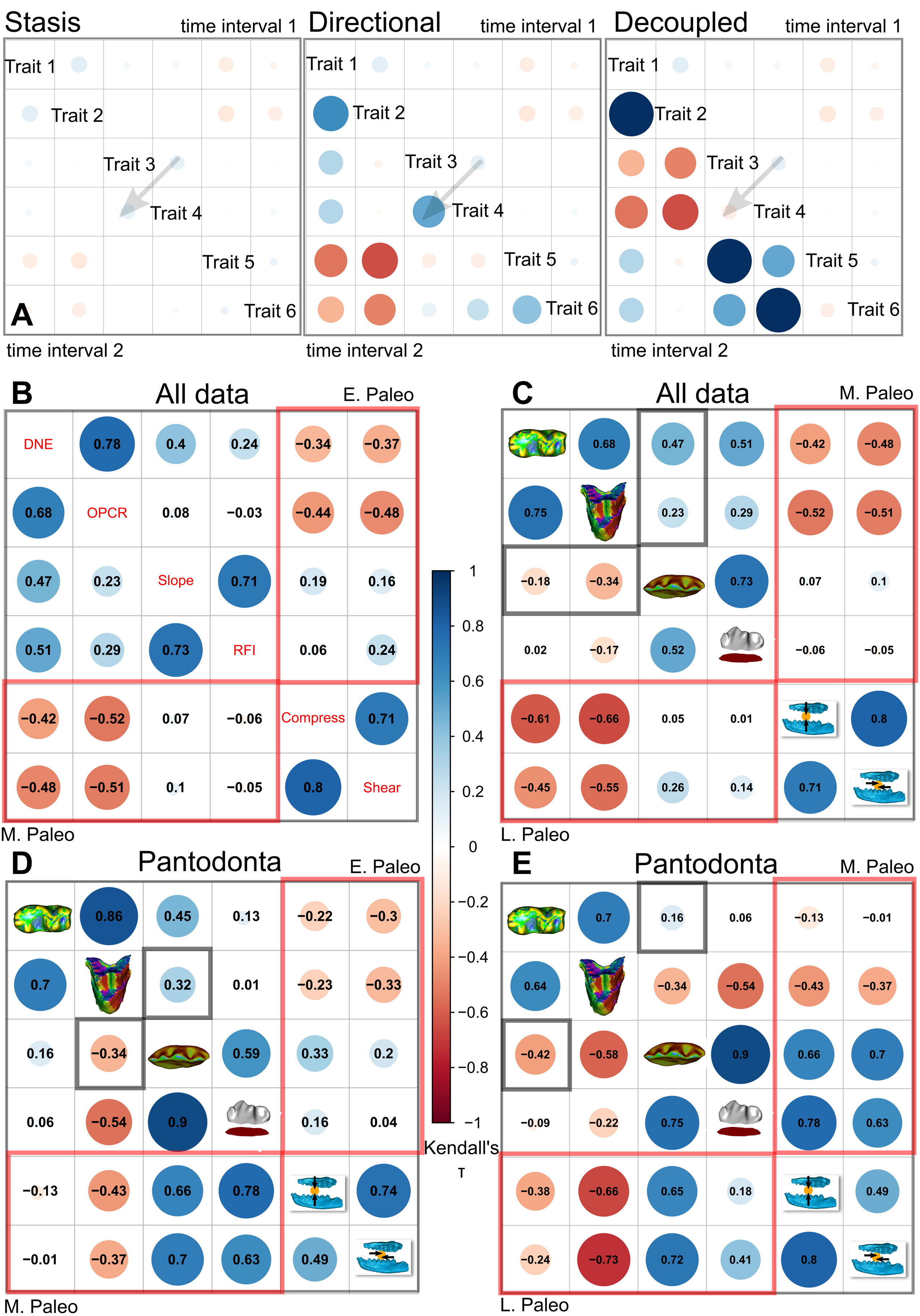
Stasis
time interval 1
time interval 2
Directional
time interval 1
time interval 2
Decoupled
time interval 1
time interval 2
Trait 1
Trait 2
Trait 3
Trait 4
Trait 5
Trait 6
A
B
All data
E. Paleo
M. Paleo
DNE 0.78 0.4 0.24 −0.34 −0.37
0.68 OPCR 0.08 −0.03 −0.44 −0.48
0.47 0.23 Slope 0.71 0.19 0.16
0.51 0.29 0.73 RFI 0.06 0.24
−0.42 −0.52 0.07 −0.06 Compress 0.71
−0.48 −0.51 0.1 −0.05 0.8 Shear
C
All data
M. Paleo
L. Paleo
0.68 0.47 0.51 −0.42 −0.48
0.75 0.23 0.29 −0.52 −0.51
−0.18 −0.34 0.73 0.07 0.1
0.02 −0.17 0.52 −0.06 −0.05
−0.61 −0.66 0.05 0.01 0.8
−0.45 −0.55 0.26 0.14 0.71
D
Pantodonta
E. Paleo
M. Paleo
0.86 0.45 0.13 −0.22 −0.3
0.7 0.32 0.01 −0.23 −0.33
0.16 −0.34 0.59 0.33 0.2
0.06 −0.54 0.9 0.16 0.04
−0.13 −0.43 0.66 0.78 0.74
−0.01 −0.37 0.7 0.63 0.49
E
Pantodonta
M. Paleo
L. Paleo
0.7 0.16 0.06 −0.13 −0.01
0.64 −0.34 −0.54 −0.43 −0.37
−0.42 −0.58 0.9 0.66 0.7
−0.09 −0.22 0.75 0.78 0.63
−0.38 −0.66 0.65 0.18 0.49
−0.24 −0.73 0.72 0.41 0.8
1
0.8
0.6
0.4
0.2
0
−0.2
−0.4
−0.6
−0.8
−1
Kendall's τ